

Photon-photon interaction mediated by a virtual photon in a nonlinear microcavity

Mengdi Zhao^{1, 2, 3} and Kejie Fang^{1, 3, 4, *}

¹*Holonyak Micro and Nanotechnology Laboratory,*

University of Illinois at Urbana-Champaign, Urbana, IL 61801 USA

²*Department of Physics, University of Illinois at Urbana-Champaign, Urbana, IL 61801 USA*

³*Illinois Quantum Information Science and Technology Center,*

University of Illinois at Urbana-Champaign, Urbana, IL 61801 USA

⁴*Department of Electrical and Computer Engineering,*

University of Illinois at Urbana-Champaign, Urbana, IL 61801 USA

Interactions between single photons play a crucial role in both fundamental physics and quantum technologies. So far, only a few demonstrations of photon interactions have been accomplished using quantum emitters that are strongly coupled to optical cavities or excited to Rydberg states. In this study, we achieve photon-photon interaction without the use of quantum emitters for the first time, in a monolithic waveguide-coupled microcavity with intrinsic $\chi^{(2)}$ nonlinearity and engineered dissipation. The photon interaction is mediated by a virtual photon, which is the quantum fluctuation of the vacuum. This leads to strong quantum correlations between transported photons, exhibiting repulsive, attractive, or tunneling behavior. Our work presents a novel approach to harnessing highly-engineerable bulk optical nonlinearities for controlling quantum light at the single-photon level, which has far-reaching implications for nonlinear optical quantum information processing and quantum networking.

Nonlinear optics that utilizes higher-order susceptibilities of materials, such as $\chi^{(2)}$ and $\chi^{(3)}$, has a wide range of applications, from spectroscopy to communications. In the context of quantum information processing, bulk optical nonlinearity is mainly used as a resource for parametric generation of squeezed light and entangled photon pairs for linear optical quantum computing [1, 2] and quantum networking applications [3]. Recently, cascaded parametric processes have been observed at an intermediate single-photon pump level [4, 5], resulting in entangled triplet states [6, 7]. However, a significant challenge remains to achieve direct interactions between individual photons via bulk optical nonlinearity without photon annihilation. This is crucial for several nonlinear optical quantum information processing schemes [8–13]. Currently, photon-photon interactions have only been demonstrated in a limited number of quantum systems, including trapped neutral atoms strongly coupled to optical cavities [14, 15], solid-state quantum emitters [16, 17], and Rydberg atomic gases [18–20]. However, these atomic systems are limited by stringent experimental conditions and the available photon wavelength and bandwidth, which pose difficulties in upscaling and practical applications. The use of monolithic bulk nonlinearity for photon-photon interactions allows for ambient condition operations and a high degree of control over the wavelength and bandwidth of the light.

In this study, we investigate the inherent nonlinear interaction between photons in a monolithic photonic integrated circuit possessing a significant $\chi^{(2)}$ nonlinearity. We utilize the virtual photon process and dissipation engineering technique [21] to produce strongly correlated quantum light. While virtual photons are relevant to the

scattering of charged particles in quantum electrodynamics [22], they have not yet been observed in the mediation of photon scattering. In principle, a doubly-resonant $\chi^{(2)}$ nonlinear cavity can generate photon-photon interactions comparable to those observed in a two-level system that is strongly coupled to an electromagnetic mode (Fig. 1a). The light-matter interaction in the latter case hybridizes atomic states and photon number states, resulting in an anharmonicity in the dressed state space. This anharmonicity is the basis of photon blockade [23]. In the case of a doubly-resonant $\chi^{(2)}$ nonlinear cavity, the interaction Hamiltonian is given by

$$\hat{H}_{\text{int}} = \hbar g(\hat{a}^\dagger \hat{b} + \hat{a}^2 \hat{b}^\dagger), \quad (1)$$

where $\hat{a}^\dagger(\hat{b}^\dagger)$ and $\hat{a}(\hat{b})$ are the creation and annihilation operators for the fundamental (second-harmonic) resonance, respectively, and g is the single-photon nonlinear coupling. In this scenario, the state $|1_b\rangle$ behaves like $|e\rangle$ for the two-photon transition (Fig. 1b). The $\chi^{(2)}$ -mediated nonlinear mode interaction causes an anharmonicity in the Hilbert space consisting of $|n_a m_b\rangle$ [24], and, in particular, the states $|2_a 0_b\rangle$ and $|0_a 1_b\rangle$ hybridize to form a closed subspace with a frequency splitting of $2\sqrt{2}g$. When the anharmonicity is greater than the photon dissipation κ , it is possible to achieve deterministic quantum logic gates by exploiting the $\chi^{(2)}$ nonlinearity [8–11]. However, as demonstrated in this study, even in the dissipation-dominated regime, the $\chi^{(2)}$ nonlinearity still produces correlated two-photon transport in the waveguide coupled with the $\chi^{(2)}$ cavity, and induces strong quantum correlations of the transported photons via virtual nonlinear processes.

The transport of few photons through a waveguide-coupled open quantum system can be described using the S –matrix formalism [25–27]. The two-photon scat-

* kfang3@illinois.edu

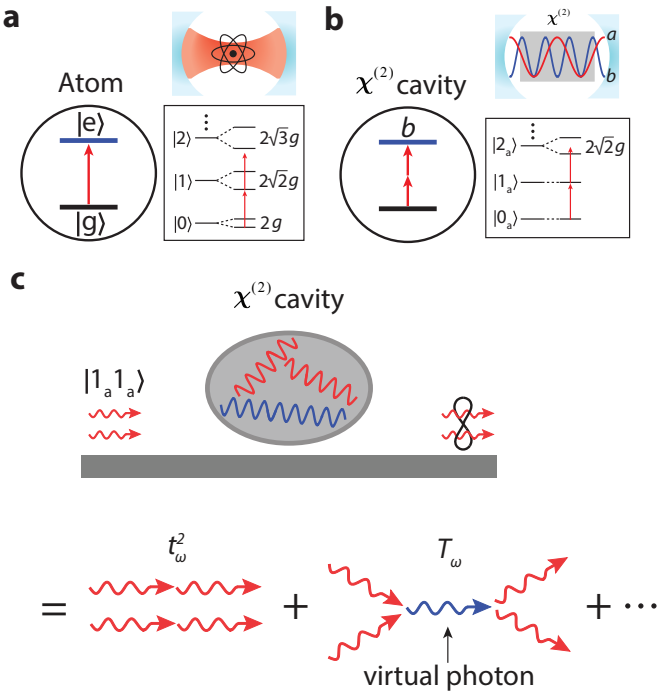


FIG. 1. **Two-photon transport via a waveguide-coupled $\chi^{(2)}$ cavity.** **a** and **b**. Analogy between the cavity-coupled two-level system (**a**) and doubly resonant $\chi^{(2)}$ cavity (**b**). Insets show the anharmonic levels of dressed states. **c**. Diagrammatic representation of the two-photon transport via a waveguide-coupled $\chi^{(2)}$ cavity, involving quantum interference between the uncorrelated transport and virtual photon-mediated scattering.

tering amplitude, $S_{\nu_1\nu_2;\omega_1\omega_2} \equiv \langle \nu_1\nu_2 | \omega_1\omega_2 \rangle_{\text{in}}$, can be expressed as [27]

$$S_{\nu_1\nu_2;\omega_1\omega_2} = S_{\nu_1\nu_2;\omega_1\omega_2}^0 + iT_{\nu_1\nu_2;\omega_1\omega_2}, \quad (2)$$

where ω_i and ν_i represent the (angular) frequency of the incoming and outgoing photons in the waveguide, respectively. The uncorrelated transport amplitude, $S_{\nu_1\nu_2;\omega_1\omega_2}^0$, is given by the product of single-photon transmission coefficients of the two photons, while the interaction-induced, correlated transport amplitude is $iT_{\nu_1\nu_2;\omega_1\omega_2}$ (see Methods). Figure 1c illustrates this process for a $\chi^{(2)}$ cavity, where correlated transport, to the leading order, is mediated by a virtual second-harmonic photon in the cavity due to the quantization of the cavity mode [22]. During this process, the two incoming photons exchange energy via the virtual photon while preserving the total energy, i.e., $\hbar\nu_1 + \hbar\nu_2 = \hbar\omega_1 + \hbar\omega_2$ (for arbitrary $\nu_{1(2)}$), leading to a two-photon scattered state with frequency entanglement. The fact that the second-harmonic photon is *virtual*, i.e., due to quantum fluctuations of the vacuum, allows photon-photon interaction to occur within the cavity-photon lifetime, even in the weak coupling regime ($g/\kappa \ll 1$). Otherwise, for the process $|2_a0_b\rangle \rightarrow |0_a1_b\rangle \rightarrow |2_a0_b\rangle$ involving a *real*

second-harmonic photon, it would take a time of $\pi/\sqrt{2}g$ corresponding to the full Rabi oscillation between $|2_a0_b\rangle$ and $|0_a1_b\rangle$, which is much longer than the cavity-photon lifetime $\sim 1/\kappa$ and cannot occur in the weak coupling regime. This virtual nonlinear process is distinct from the concept of coherent photon conversion in a nonlinear continuum [8], which involves the generation of a real second-harmonic photon and thus requires strong coupling to realize.

The second-order correlation function of transported photons for monochromatic input photons with a frequency ω is related to the S -matrix and can be expressed as (see Methods)

$$g^{(2)}(\tau) \equiv \frac{|\psi_2(t, t + \tau)|^2}{|\psi_1(t)|^4} = \frac{|t_\omega^2 + T(\omega, \tau)|^2}{|t_\omega^2|^2}, \quad (3)$$

where $\psi_2(t, t + \tau)$ and $\psi_1(t)$ denote the two-photon and single-photon wavefunction, respectively, t_ω is the single-photon transmission coefficient, and the virtual photon-scattering amplitude is given by

$$T(\omega, \tau) = -\frac{g^2 \kappa_{ae}^2}{(2\omega - \alpha_b)(\omega - \alpha_a)^3} e^{-i|\tau|(\alpha_a - \omega)} \quad (4)$$

with $\alpha_{a(b)} = \omega_{a(b)} - i\frac{\kappa_{a(b)}}{2}$. It is worth noting that $T(\omega, \tau)$ also represents the wavefunction of the interaction-induced two-photon bound state, which has a temporal extent of $1/\kappa_a$ [28]. The correlation of the transported photons is determined by the quantum interference between the scattered and unscattered transport. Even in the weak coupling regime, we can generate strongly correlated photons by controlling the single-photon transmission of the photonic circuit through, for example, the dissipation of the cavity photon. Furthermore, when t_ω^2 and $T(\omega, \tau)$ are independent, as they are in this work, we can tune the system across an extremely rich space of accessible photon correlations.

Our experiment utilizes the $\chi^{(2)}$ InGaP photonic platform with a high nonlinearity-to-loss ratio [29]. The fabricated InGaP photonic circuit, which is wavelength-multiplexed with multiple microrings of slightly different widths, is shown in scanning electron microscope images in Fig. 2a (see Methods and Supplementary Information (SI) for fabrication and device details). The nominal microring resonator is designed to support phase- and frequency-matched fundamental 1550-nm-band transverse-electric (TE₀₀) and second-harmonic 775-nm-band transverse-magnetic (TM₀₀) resonances for $\chi^{(2)}$ -enabled photon interaction. For standing-wave ring resonances, the cavity photon dissipation can be tuned via a terminated-waveguide feedback as shown in Fig. 2b. The tunable cavity dissipation is approximately given by $\kappa_{ae} = \frac{1}{2}\kappa_{e0}(1 - \sin 2\varphi)$, where κ_{e0} is the original external cavity dissipation and φ is the waveguide phase between the microring and the photonic crystal mirror [30] (SI). Via an integrated resistive heater, we can tune the waveguide phase φ and therefore the single-photon transmis-

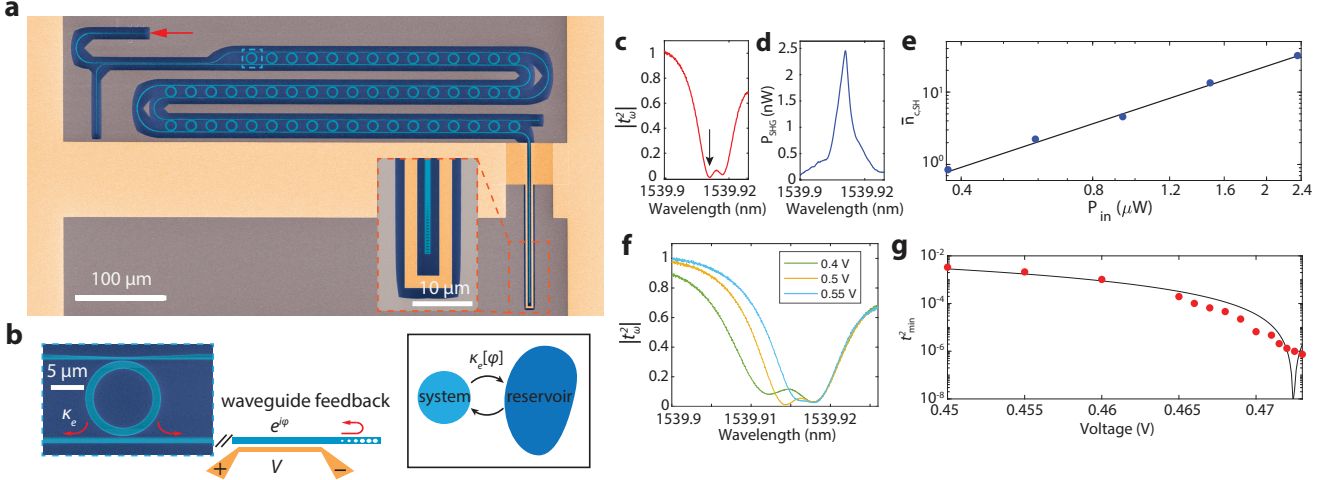


FIG. 2. Dissipation-engineered nonlinear photonic circuit. **a.** False-color scanning electron microscope images of the fabricated photonic circuit. Inset shows the photonic crystal mirror-terminated waveguide and the resistive phase shifter (yellow). **b.** Dissipation engineering of the microring resonator via the waveguide feedback. The cavity-photon dissipation into the waveguide is controlled by the waveguide phase φ . **c.** Normalized transmission spectrum of the phase- and frequency-matched resonance (arrow) used in the experiment. **d.** Second-harmonic power spectrum. **e.** Second-harmonic cavity photon number for varying input power at 1539.914 nm. Solid line is the model fitting. **f.** Tuning of the transmission spectrum of the phase-matched resonance for various applied voltages. **g.** Fine-tuning of the minimum transmission at 1539.914 nm. Solid line is the model fitting (SI).

sion coefficient of the one-port photonic circuit, which depends on κ_{ae} . The waveguide feedback also induces a frequency detuning, Δ , between the local minimum of the transmission spectrum and the bare cavity resonance, which is related to the creation of photon repulsion.

Fig. 2c shows the spectrum of a pair of split 1550-nm band TE₀₀ standing-wave resonances of a microring resonator. The intrinsic quality factors of the 1550-nm band TE₀₀ resonance and 775-nm band TM₀₀ resonance are typically about $Q_{ai} \approx 2.5 \times 10^5$ and $Q_{bi} \approx 5 \times 10^4$, respectively. To characterize the nonlinear mode coupling g , we used the process of second harmonic generation (SHG). The 1550-nm-band TE₀₀ resonance that satisfies the frequency- and phase-matching condition with a 775-nm-band TM₀₀ resonance of the same microring allows for strong SHG. Fig. 2d shows the measured second-harmonic signal from the phase-matched resonance around 1539.914 nm for an input laser power of $P_{in} = 1.49 \mu\text{W}$. For this resonance, the inferred second-harmonic cavity photon number $\bar{n}_{c,\text{SH}}$ for varying input power is plotted in Fig. 2e, leading to an SHG efficiency of $105000 \pm 13360\%/\text{W}$. The nonlinear mode coupling is extracted from the SHG efficiency to be $g/2\pi = 6.5 \text{ MHz}$ (SI), resulting in a nonlinearity-to-loss ratio of $g/\kappa_{ai} = 0.84\%$ or $g/\sqrt{\kappa_{ai}\kappa_{bi}} = 0.27\%$.

The measurement of photon correlations is carried out at a temperature of 4 K in order to reduce the effects of thermomechanical noise originating from the vibrational modes of the membrane device and thermorefractive noise [30]. Nevertheless, operating the device at room temperature is possible by utilizing the InGaP-on-

insulator architecture [31], which avoids low-frequency vibrational modes and exhibits high thermal conductance. Prior to coupling the laser into the device, it is filtered to eliminate amplified spontaneous emission, side-mode emission, and unpolarized light (SI). Correlations of the transmitted light are measured in a Hanbury Brown-Twiss setup. The phase-matched resonance at 1539.914 nm can be tuned from under-coupling ($\kappa_{ai} > \kappa_{ae}$) to over-coupling ($\kappa_{ai} < \kappa_{ae}$) with a tuning voltage of less than 1 V at 4 K (Fig. 2f). In the vicinity of the critical-coupling regime ($V \approx 0.47 \text{ V}$), the local minimum of the transmission spectrum, t_{\min}^2 , can be precisely tuned with a resolution of about 10^{-6} using voltage increments of 1 mV (Fig. 2g). The minimum achievable value of t_{\min}^2 is limited by residual thermomechanical noise (SI).

We perform measurements using a weak coherent field with frequency around the local transmission minimum at 1539.914 nm as the input signal of the photonic circuit. The power of the weak coherent field satisfies the weak driving condition, i.e., $\bar{n}_{c,\text{SH}} \approx 4(g\bar{n}_c/\kappa_b)^2 < 1$, such that the single-photon nonlinearity is not saturated. In our experiment, the on-chip input optical power is $P_{in} = 56.3 \text{ nW}$, corresponding to a cavity photon number $\bar{n}_c = 89$ and a cavity second-harmonic photon number $\bar{n}_{c,\text{SH}} = 0.021$. The two-photon component of the weak coherent state is subject to the $\chi^{(2)}$ -enabled interaction in the cavity, leading to second-order quantum correlations of the transmitted light given by Eq. 3 (SI). The quantum correlation of transmitted photons can be controlled by the signal-local minimum detuning, δ , and the waveguide phase, φ , which sets the local minimum

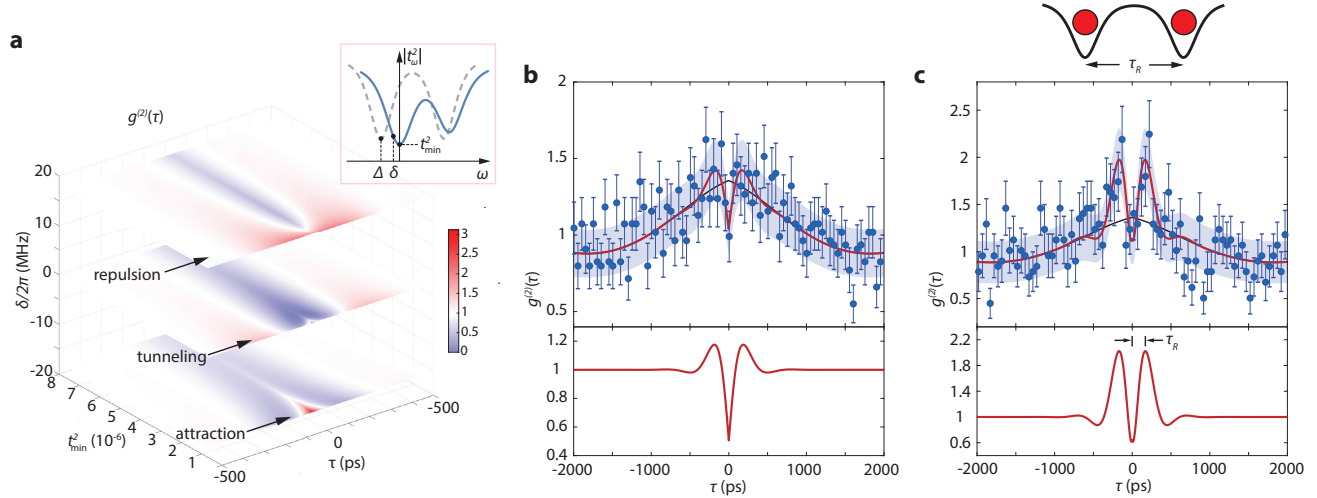


FIG. 3. Tunable quantum correlations and photon repulsion. **a.** Calculated $g^{(2)}(\tau)$ for various t_{\min}^2 and δ . Inset illustrates the parameters used to control $g^{(2)}(\tau)$. Blue line is the transmission spectrum $|t_\omega|^2$ and dashed line is the bare cavity resonances. **b** and **c.** Measured $g^{(2)}(\tau)$ of transported photons, which show features of antibunching and photon repulsion. Red line is model fitting of the data. Black line is fitting of the thermomechanical noise background. Bottom panel shows fitted signal subtracted by the thermomechanical noise background. The shaded area and error bar represents \pm one standard deviation of the fitted line (red) and measured data, respectively. See SI for fitting details.

transmission, t_{\min}^2 , and the local minimum-cavity resonance detuning, Δ (Fig. 3a inset). Fig. 3a shows the theoretical calculation of $g^{(2)}(\tau)$ for various t_{\min}^2 and δ with $\Delta \approx \kappa_a$ and practical device parameters, indicating regimes with distinctive correlation features corresponding to photon attraction, repulsion, and quantum tunneling.

We maintain the local minimum of the transmission spectrum within the range of $6-9 \times 10^{-7}$. The measured correlations $g^{(2)}(\tau)$ for single-photon transmission coefficients $|t_\omega|^2 = (5.6 \pm 1.4) \times 10^{-6}$ and $(3.9 \pm 1.2) \times 10^{-6}$ are shown in Fig. 3b and c, respectively. The red line in the figures represents the model fitting (SI). The distinct features of $g^{(2)}(\tau)$ in the range $|\tau| \lesssim 2\pi/\kappa_a (\approx 500 \text{ ps})$ are due to the photon-photon interaction in the $\chi^{(2)}$ cavity with a bandwidth of $\kappa_a/2\pi$. The weak bunching effect ($g^{(2)} > 1$) at a much larger time scale is due to the residual thermomechanical noise at 4 K [30], which is universal for all ring resonances (see SI for the measured $g^{(2)}(\tau)$ of a phase-unmatched resonance). In Fig. 3b, an antibunching effect is observed where $g^{(2)}(0) < g^{(2)}(\tau)$ for the transported photons (after noise subtraction, $g^{(2)}(0) \approx 0.5$), indicating a suppressed likelihood of finding two photons at $\tau = 0$. The cause of this antibunching effect is attributed to the swap between the two incoming photons and the virtual second-harmonic photon, occurring within the time interval $1/\kappa_a$, which leads to a π phase shift of the scattered state and cancellation with the unscattered amplitude. Additionally, an effective repulsive interaction between photons is observed, characterized by a peaked correlation $g^{(2)} > 1$ at a finite delay $\tau_R (\approx 200 \text{ ps})$, indicating that the two photons are pushed away from each other with a temporal separation τ_R .

The appearance of the peaked $g^{(2)}(\tau)$ at τ_R is attributed to the detuning between the signal and bare cavity resonance, $|\Delta - \delta|$, which leads to an oscillation of $T(\omega, \tau)$ with a period $2\pi/|\Delta - \delta|$ (see Eq. 7) and thus constructive interference between t_ω^2 and $T(\omega, \tau)$ at the half period $\tau_R \sim \pi/|\Delta - \delta|$. It is necessary to have $\Delta \gtrsim \kappa_a$ to observe the photon repulsion since $T(\omega, \tau)$ has a decay rate of κ_a . The photonic circuit architecture with split standing-wave resonances and tunable waveguide feedback makes this possible for the observed resonance, with $\Delta/2\pi \approx 1.6 \text{ GHz}$ as found from model fitting and $|\delta|/2\pi \approx 1-3 \text{ MHz}$.

When the input photon frequency approaches the local minimum of the transmission spectrum, the two-photon wavefunction is dominated by the $\chi^{(2)}$ interaction-induced amplitude $T(\omega, \tau)$. As a result, $g^{(2)}$ shows features of the two-photon bound state [18, 28]. Fig. 4a shows the measured correlation $g^{(2)}(\tau)$ at $|t_\omega|^2 = (3.7 \pm 1.1) \times 10^{-6}$, during the transition from photon repulsion to attraction. Fig. 4b shows the bound state at $|t_\omega|^2 = (2.9 \pm 1.0) \times 10^{-6}$ characterized by $g^{(2)}(0) = 2.98 \pm 0.68$ ($g^{(2)}(0) \approx 4.3$ after noise subtraction) and $g^{(2)}(0) > g^{(2)}(\tau)$, meaning the two photons are attracted to each other with increased likelihood of being found together. Remarkably, besides the photon attraction and repulsion, Fig. 4a exhibits positive correlations ($g^{(2)} > 1$) at zero delay and finite delay with anti-correlation ($g^{(2)} < 1$) between the peaks. The physical meaning of this distinctive second-order correlation can be explained by the tunneling of the photon across the potential barrier of the repulsive interaction. In contrast to the cascaded

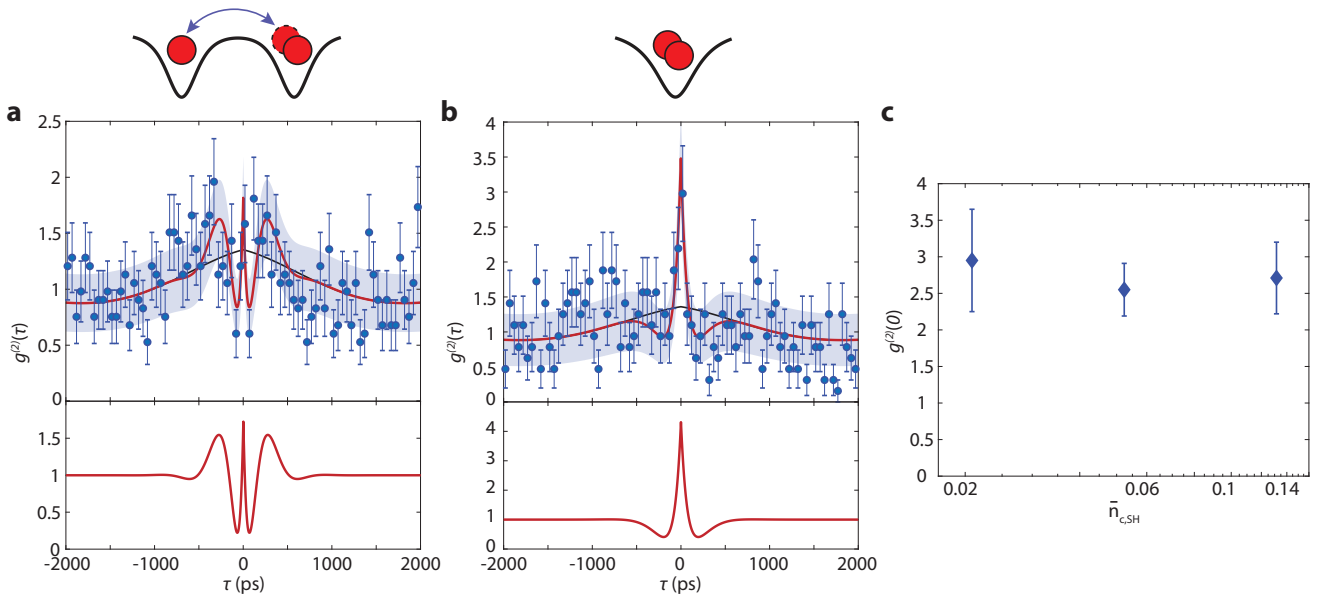


FIG. 4. **Photon attraction and two-photon bound state.** **a.** Measured $g^{(2)}(\tau)$ showing a quantum tunneling effect of photons. **b.** Measured $g^{(2)}(\tau)$ showing attractive interaction between photons, leading to the two-photon bound state. **c.** $g^{(2)}(0)$ of the two-photon bound state for various $\bar{n}_{c,SH}$ in the weak driving regime.

process of SHG with real second-harmonic photons and parametric down-conversion, where the bunching effect of the down-converted photons is associated with a correlation $g^{(2)}(0)$ inversely proportional to the SHG power as a purely statistical effect, here the zero-time $g^{(2)}(0)$ of the bound state due to the virtual photon-mediated interaction is independent of the input optical power. We observed an unchanged $g^{(2)}(0)$ at the same $|t_\omega|^2$ for three different $\bar{n}_{c,SH}$ satisfying the weak driving condition, as shown in Fig. 4c.

Our experimental findings present a novel method for generating strongly-correlated photons in nonlinear optical systems without requiring strong light-matter interaction or quantum emitters. The implications of our results are far-reaching, especially in the field of quantum information processing and quantum networking. For instance, the $\chi^{(2)}$ -mediated photon interaction (between two different fundamental modes) can facilitate quan-

tum non-demolition measurement of photons [32], which is crucial for repeater-enabled quantum networks [33]. With the possibility of reducing photon losses [34] and engineering material nonlinearity [35–37], the strong coupling regime ($g > \kappa$) in monolithic photonic platforms is within reach for nonlinearity-enabled optical quantum information processing [8–11]. Additionally, our approach can be extended to other bulk nonlinearities such as electro-optic and optomechanical systems, enabling the creation of quantum correlations of bosonic excitations across a broad electromagnetic spectrum beyond the direct transduction scheme [38].

Methods

Two-photon S –matrix and quantum correlations

The few-photon scattering amplitude can be calculated using a diagrammatic approach [25] and, for the case of two incoming photons in the fundamental mode a , the result is given by (SI)

$$S_{\nu_1 \nu_2; \omega_1 \omega_2} \approx t_{\omega_1} t_{\omega_2} [\delta(\nu_1 - \omega_1) \delta(\nu_2 - \omega_2) + \delta(\nu_1 - \omega_2) \delta(\nu_2 - \omega_1)] - \frac{2ig^2}{\pi} \frac{\kappa_{ae}^2}{(\omega_1 - \alpha_a)(\omega_2 - \alpha_a)(\nu_1 - \alpha_a)(\nu_2 - \alpha_a)(\omega_1 + \omega_2 - \alpha_b)} \delta(\nu_1 + \nu_2 - \omega_1 - \omega_2). \quad (5)$$

Only the leading-order term of $iT_{\nu_1 \nu_2; \omega_1 \omega_2}$ is included in Eq. 5, which corresponds to the amplitude of two-photon scattering mediated by a virtual sum-frequency photon. The full expression of the S –matrix including higher-order interaction terms is provided in SI. For monochro-

matic input photons with frequency ω , the temporal two-photon wavefunction of the transported photons is re-

lated to the S -matrix by

$$\begin{aligned}\psi_2(t, t + \tau) &= \int d\nu_1 d\nu_2 S_{\nu_1 \nu_2; \omega\omega} e^{-i\nu_1 t - i\nu_2(t + \tau)} \\ &= e^{-i\omega(2t + \tau)} [t_\omega^2 + T(\omega, \tau)],\end{aligned}\quad (6)$$

where t_ω is the single-photon transmission coefficient and

$$T(\omega, \tau) = -\frac{g^2 \kappa_{ae}^2}{(2\omega - \alpha_b)(\omega - \alpha_a)^3} e^{-i|\tau|(\alpha_a - \omega)}. \quad (7)$$

The second-order correlation function thus is given by $g^{(2)}(\tau) \equiv \frac{|\psi_2(t, t + \tau)|^2}{|\psi_1(t)|^4}$, where $\psi_1(t) = e^{-i\omega t} t_\omega$ is the single-photon wavefunction. For the split-resonance cavity with waveguide feedback, the single-photon transmission near the local transmission minimum can be modeled as $t_\omega = r - \frac{i\kappa_{a,e}}{\omega - \omega_{\min} + i\kappa_a/2}$, where ω_{\min} is the frequency of the local minimum and is different from the bare cavity frequency ω_a due to the waveguide feedback.

Device fabrication The devices are fabricated from the 115 nm thick disordered $\text{In}_{0.48}\text{Ga}_{0.52}\text{P}$ thin film grown on GaAs substrate by metal-organic chemical vapor deposition. The device pattern is defined using electron beam lithography and negative tone resist hydrogen silsesquioxane. The device pattern is transferred to In-GaP layer via inductively coupled plasma reactive-ion etch (ICP-RIE) using a mixture of $\text{Cl}_2/\text{CH}_4/\text{Ar}$ gas. A layer of 35 nm thick aluminum oxide is deposited on the chip via atomic layer deposition. This layer serves as the mechanical support for the suspended device. A second electron beam lithography and subsequent ICP-RIE using CHF_3 gas are applied to pattern etch-through holes in the aluminum oxide layer for the undercut of the In-GaP device. A third electron beam lithography followed by electron-beam evaporation of 5 nm thick chromium and 20 nm thick gold is performed to define the high-resistance wires next to the 1550-nm light waveguide as the resistive phase shifter. A fourth electron beam lithography followed by electron-beam evaporation of 10 nm thick chromium and 150 nm thick gold is used to define the low-resistance large metal pads that connect the resistive heater to the wire bonding pad. Finally, the InGaP device is released from the GaAs substrate using citric acid-based selective etching.

InGaP photonic integrated circuit The design of

the phase-matched microring resonator follows Ref. [29]. The nominal ring radius is 5 μm . The microring resonator is coupled to two bus waveguides for transmitting the 1550-nm and 775-nm wavelength light, respectively. The two bus waveguides are joined at a wavelength-division multiplexer (WDM), which is then connected to a tapered fiber-optic coupler which couples both 1550-nm TE polarized and 775-nm TM polarized light from a tapered fiber into the photonic circuit with an efficiency of about 60% and 20%, respectively. At the end of the 1550-nm light waveguide, metal wires are fabricated on both sides of the waveguide in order to tune the phase of the waveguide via resistive heating and thermo-optic effect. A group of 50 microrings with width increment at 1 nm step are fabricated in one device which effectively enhances the probability to realize the phase- and frequency-matching condition of a device and simplifies the measurement.

Photon correlation measurement The device chip is wire-bonded to a printed circuit board for voltage tuning of the waveguide phase and is mounted in the mixing chamber of a dilution refrigerator (DR) operated at 4 K. A bare optical fiber is fed through the DR for transmitting light. The tapered fiber tip is glued to the on-chip waveguide coupler for low-loss, mechanically-stable fiber-optic coupling that is immune to the DR vibration. Light from a tunable external cavity diode laser (New Focus TLB-6728) is filtered by an optical grating filter (JDS TB9223, 3 dB bandwidth 0.55 nm, 20 dB bandwidth 1.5 nm) and a fiber Fabry-Perot (FP) filter (LUNA, 50 GHz free spectral range, 400 finesse) to eliminate the amplified spontaneous emission and side-mode emission of the laser. One resonance of the FP filter is locked to the laser frequency via a dither feedback controller. The filtered light is then passed through a fiber polarizer (50 dB extinction) to eliminate unpolarized light and a 1550-nm/775-nm WDM before coupling into the device. The 775-nm wavelength second-harmonic light from the device is detected by an avalanche photodetector (Thorlabs APD440A). The 1550-nm wavelength light is further purified by a polarizer (40 dB extinction) and its correlations is analyzed using the Hanbury Brown-Twiss setup which consists of a 50:50 beamsplitter, two SNSPDs (Quantum Opus), and a TCSPC (Time Tagger Ultra).

[1] Han-Sen Zhong, Hui Wang, Yu-Hao Deng, Ming-Cheng Chen, Li-Chao Peng, Yi-Han Luo, Jian Qin, Dian Wu, Xing Ding, Yi Hu, *et al.*, “Quantum computational advantage using photons,” *Science* **370**, 1460–1463 (2020).

[2] Juan M Arrazola, Ville Bergholm, Kamil Brádler, Thomas R Bromley, Matt J Collins, Ish Dhand, Alberto Fumagalli, Thomas Gerrits, Andrey Goussev, Lukas G Helt, *et al.*, “Quantum circuits with many photons on a programmable nanophotonic chip,” *Nature* **591**, 54–60 (2021).

[3] Zhen-Sheng Yuan, Xiao-Hui Bao, Chao-Yang Lu, Jun Zhang, Cheng-Zhi Peng, and Jian-Wei Pan, “Entangled photons and quantum communication,” *Physics Reports* **497**, 1–40 (2010).

[4] Hannes Hübel, Deny R Hamel, Alessandro Fedrizzi, Sven Ramelow, Kevin J Resch, and Thomas Jennewein, “Direct generation of photon triplets using cascaded photon-pair sources,” *Nature* **466**, 601–603 (2010).

[5] Thiago Guerreiro, Enrico Pomarico, Bruno Sanguinetti, Nicolas Sangouard, JS Pelc, C Langrock, MM Fejer,

Hugo Zbinden, Robert T Thew, and Nicolas Gisin, "Interaction of independent single photons based on integrated nonlinear optics," *Nature Communications* **4**, 1–5 (2013).

[6] Lynden K Shalm, Deny R Hamel, Zhizhong Yan, Christoph Simon, Kevin J Resch, and Thomas Jennewein, "Three-photon energy–time entanglement," *Nature Physics* **9**, 19–22 (2013).

[7] Deny R Hamel, Lynden K Shalm, Hannes Hübel, Aaron J Miller, Francesco Marsili, Varun B Verma, Richard P Mirin, Sae Woo Nam, Kevin J Resch, and Thomas Jennewein, "Direct generation of three-photon polarization entanglement," *Nature Photonics* **8**, 801–807 (2014).

[8] Nathan K Langford, Sven Ramelow, Robert Prevedel, William J Munro, Gerard J Milburn, and Anton Zeilinger, "Efficient quantum computing using coherent photon conversion," *Nature* **478**, 360–363 (2011).

[9] Murphy Yuezhen Niu, Isaac L Chuang, and Jeffrey H Shapiro, "Qudit-basis universal quantum computation using $\chi^{(2)}$ interactions," *Physical Review Letters* **120**, 160502 (2018).

[10] Ming Li, Yan-Lei Zhang, Hong X Tang, Chun-Hua Dong, Guang-Can Guo, and Chang-Ling Zou, "Photon–photon quantum phase gate in a photonic molecule with $\chi^{(2)}$ nonlinearity," *Physical Review Applied* **13**, 044013 (2020).

[11] Stefan Krastanov, Mikkel Heuck, Jeffrey H Shapiro, Prineha Narang, Dirk R Englund, and Kurt Jacobs, "Room-temperature photonic logical qubits via second-order nonlinearities," *Nature Communications* **12**, 1–10 (2021).

[12] Adi Pick, ES Matekole, Ziv Aqua, Gabriel Guendelman, Ofer Firstenberg, Jonathan P Dowling, and Barak Dayan, "Boosting photonic quantum computation with moderate nonlinearity," *Physical Review Applied* **15**, 054054 (2021).

[13] Ryotatsu Yanagimoto, Edwin Ng, Marc Jankowski, Hideo Mabuchi, and Ryan Hamerly, "Temporal trapping: a route to strong coupling and deterministic optical quantum computation," *Optica* **9**, 1289–1296 (2022).

[14] Quentin A Turchette, Christina J Hood, Wolfgang Lange, Hideo Mabuchi, and H Jeff Kimble, "Measurement of conditional phase shifts for quantum logic," *Physical Review Letters* **75**, 4710 (1995).

[15] Bastian Hacker, Stephan Welte, Gerhard Rempe, and Stephan Ritter, "A photon–photon quantum gate based on a single atom in an optical resonator," *Nature* **536**, 193–196 (2016).

[16] Ilya Fushman, Dirk Englund, Andrei Faraon, Nick Stoltz, Pierre Petroff, and Jelena Vuckovic, "Controlled phase shifts with a single quantum dot," *Science* **320**, 769–772 (2008).

[17] Hanna Le Jeannic, Alexey Tiranov, Jacques Carolan, Tomás Ramos, Ying Wang, Martin Hayhurst Appel, Sven Scholz, Andreas D Wieck, Arne Ludwig, Nir Rotenberg, *et al.*, "Dynamical photon–photon interaction mediated by a quantum emitter," *Nature Physics* **18**, 1191–1195 (2022).

[18] Ofer Firstenberg, Thibault Peyronel, Qi-Yu Liang, Alexey V Gorshkov, Mikhail D Lukin, and Vladan Vuletić, "Attractive photons in a quantum nonlinear medium," *Nature* **502**, 71–75 (2013).

[19] Daniel Tiarks, Steffen Schmidt-Eberle, Thomas Stoltz, Gerhard Rempe, and Stephan Dürr, "A photon–photon quantum gate based on Rydberg interactions," *Nature Physics* **15**, 124–126 (2019).

[20] Sergio H Cantu, Aditya V Venkatramani, Wenchao Xu, Leo Zhou, Brana Jelenković, Mikhail D Lukin, and Vladan Vuletić, "Repulsive photons in a quantum nonlinear medium," *Nature Physics* **16**, 921–925 (2020).

[21] Patrick M Harrington, Erich J Mueller, and Kater W Murch, "Engineered dissipation for quantum information science," *Nature Reviews Physics* **4**, 660–671 (2022).

[22] Michael E Peskin, *An introduction to quantum field theory* (CRC Press, Boca Raton, 2018).

[23] Kevin M Birnbaum, Andreea Boca, Russell Miller, Allen D Boozer, Tracy E Northup, and H Jeff Kimble, "Photon blockade in an optical cavity with one trapped atom," *Nature* **436**, 87–90 (2005).

[24] Arka Majumdar and Dario Gerace, "Single-photon blockade in doubly resonant nanocavities with second-order nonlinearity," *Physical Review B* **87**, 235319 (2013).

[25] Yunkai Wang and Kejie Fang, "Few-photon transport via a multimode nonlinear cavity: theory and applications," *Physical Review A* **105**, 023713 (2022).

[26] Shanshan Xu and Shanhui Fan, "Input-output formalism for few-photon transport: A systematic treatment beyond two photons," *Physical Review A* **91**, 043845 (2015).

[27] Shanshan Xu, Eden Rephaeli, and Shanhui Fan, "Analytic properties of two-photon scattering matrix in integrated quantum systems determined by the cluster decomposition principle," *Physical Review Letters* **111**, 223602 (2013).

[28] Jung-Tsung Shen and Shanhui Fan, "Strongly correlated two-photon transport in a one-dimensional waveguide coupled to a two-level system," *Physical Review Letters* **98**, 153003 (2007).

[29] Mengdi Zhao and Kejie Fang, "InGaP quantum nanophotonic integrated circuits with 1.5% nonlinearity-to-loss ratio," *Optica* **9**, 258–263 (2022).

[30] Mengdi Zhao and Kejie Fang, "Observation of photon–phonon correlations via dissipative filtering," *Physical Review Applied* **18**, 034043 (2022).

[31] Aude Martin, Dorian Sanchez, Sylvain Combré, Alfredo De Rossi, and Fabrice Raineri, "GaInP on oxide nonlinear photonic crystal technology," *Optics Letters* **42**, 599–602 (2017).

[32] Keyu Xia, Mattias Johnsson, Peter L Knight, Jason Twamley, *et al.*, "Cavity-free scheme for nondestructive detection of a single optical photon," *Physical Review Letters* **116**, 023601 (2016).

[33] Christoph Simon, "Towards a global quantum network," *Nature Photonics* **11**, 678–680 (2017).

[34] Weiqiang Xie, Lin Chang, Haowen Shu, Justin C Norman, Jon D Peters, Xingjun Wang, and John E Bowers, "Ultrahigh-Q AlGaAs-on-insulator microresonators for integrated nonlinear photonics," *Optics Express* **28**, 32894–32906 (2020).

[35] Emmanuel Rosencher, Andrea Fiore, Borge Vinter, V Berger, Ph Bois, and J Nagle, "Quantum engineering of optical nonlinearities," *Science* **271**, 168–173 (1996).

[36] Juanjuan Lu, Ming Li, Chang-Ling Zou, Ayed Al Sayem, and Hong X Tang, "Toward 1% single-photon anharmonicity with periodically poled lithium niobate microring resonators," *Optica* **7** (2020).

[37] Ping Wang, Ding Wang, Shubham Mondal, Mingtao Hu, Jiangnan Liu, and Zetian Mi, "Dawn of nitride ferroelec-

tric semiconductors: from materials to devices,” Semiconductor Science and Technology **38**, 043002 (2023).

[38] Nikolai Lauk, Neil Sinclair, Shabir Barzanjeh, Jacob P Covey, Mark Saffman, Maria Spiropulu, and Christoph Simon, “Perspectives on quantum transduction,” Quantum Science and Technology **5**, 020501 (2020).

Data availability

Data supporting the findings of this study are available within the article and its Supplementary Information, or from the corresponding author upon reasonable request.

Acknowledgements

We acknowledge the help from Siyuan Wang and Hao

Tong during the device fabrication. We also thank Elizabeth Goldschmidt and Paul Kwiat for valuable discussions. This work was supported by US National Science Foundation (Grant No. DMS-1839177, ECCS-2223192) and U.S. Department of Energy Office of Science National Quantum Information Science Research Centers.

Author contributions

K.F. conceived the experiment. M.Z. fabricated the device. M.Z. and K.F. performed the experiment and analyzed the result. K.F. wrote the manuscript with the input from M.Z..

Supplementary Information for: “Photon-photon interaction mediated by a virtual photon in a nonlinear microcavity”

Mengdi Zhao^{1, 2, 3} and Kejie Fang^{1, 3, 4, *}

¹*Holonyak Micro and Nanotechnology Laboratory,*

University of Illinois at Urbana-Champaign, Urbana, IL 61801 USA

²*Department of Physics, University of Illinois at Urbana-Champaign, Urbana, IL 61801 USA*

³*Illinois Quantum Information Science and Technology Center,*

University of Illinois at Urbana-Champaign, Urbana, IL 61801 USA

⁴*Department of Electrical and Computer Engineering,*

University of Illinois at Urbana-Champaign, Urbana, IL 61801 USA

CONTENTS

I. Theory of two-photon transport	2
A. Computation of scattering amplitudes	2
B. Second-order correlation function	4
C. Modeling of the effective one-port photonic circuit	5
II. Device fabrication	8
III. The InGaP photonic circuit: design and characterization	9
A. On-chip wavelength-division multiplexer	10
B. Resistive phase shifter	11
IV. Experimental setup	11
V. Noise sources and mitigation	12
A. Amplified spontaneous emission, laser side modes, and unpolarized light	12
B. Thermomechanical and thermorefractive noises	12
VI. Cryogenic nonlinear photonics experiment	13
A. Frequency- and phase-matched device	13
B. Mechanically-rigid fiber-optic coupler	13
VII. Data analysis	14
A. Nonlinear mode coupling	14
B. Tuning minimum transmission	15
C. Second-order correlation function	15
References	16

* kfang3@illinois.edu

I. THEORY OF TWO-PHOTON TRANSPORT

A. Computation of scattering amplitudes

The S -matrix of few-photon transport via a waveguide-coupled nonlinear optical cavity can be systematically computed using quantum field theory methods [1, 2], including the Feynman diagram approach suitable for the weak-coupling regime, i.e., $g/\kappa < 1$. The purpose of this Section is to outline the key steps in calculation of two-photon scattering amplitude using the Feynman diagram approach. More details can be found in Ref. [2].

For a $\chi^{(2)}$ nonlinear cavity with an interaction Hamilton $H_{\text{int}} = \hbar g(a^{\dagger 2}b + a^2b^{\dagger})$ and coupled with a one-port waveguide with an input-output relation $a_{\text{out}}(t) = a_{\text{in}}(t) - i\sqrt{\kappa_{ae}}a(t)$, the time-domain S -matrix of single-photon and two-photon transport is given by

$$S_{t;t'} \equiv \langle 0 | a_{\text{out}}(t) a_{\text{in}}^{\dagger}(t') | 0 \rangle = \delta(t - t') - \kappa_{ae}G(t; t') \quad (\text{S1})$$

and

$$S_{t_1 t_2; t'_1 t'_2} \equiv \langle 0 | a_{\text{out}}(t_1) a_{\text{out}}(t_2) a_{\text{in}}^{\dagger}(t'_1) a_{\text{in}}^{\dagger}(t'_2) | 0 \rangle = \delta(t_1 - t'_1)\delta(t_2 - t'_2) + \delta(t_1 - t'_2)\delta(t_2 - t'_1) - \kappa_{ae}G(t_1; t'_1)\delta(t_2 - t'_2) - \kappa_{ae}G(t_2; t'_2)\delta(t_1 - t'_1) - \kappa_{ae}G(t_1; t'_2)\delta(t_2 - t'_1) - \kappa_{ae}G(t_2; t'_1)\delta(t_1 - t'_2) + \kappa_{ae}^2G(t_1, t_2; t'_1, t'_2), \quad (\text{S2})$$

respectively, where $G(t; t') \equiv \langle 0 | \hat{T}[a(t)a^{\dagger}(t')] | 0 \rangle$ and $G(t_1, t_2; t'_1, t'_2) \equiv \langle 0 | \hat{T}[a(t_1)a(t_2)a^{\dagger}(t'_1)a^{\dagger}(t'_2)] | 0 \rangle$ are the two-point and four-point Green's function of the cavity mode a , respectively, and \hat{T} is the time-ordering operator.

The frequency-domain S -matrix characterizing the scattering amplitude between monochromatic output and input photons is obtained by the Fourier transform of the time-domain S -matrix, i.e.,

$$S_{\nu_1; \omega_1} \equiv \mathcal{F}[S_{t;t'}] = \int \frac{dt}{\sqrt{2\pi}} e^{i\nu_1 t} \int \frac{dt'}{\sqrt{2\pi}} e^{i\omega_1 t'} S_{t;t'} = \delta(\nu_1 - \omega_1) - \kappa_{ae}G(\nu_1; \omega_1), \quad (\text{S3})$$

$$S_{\nu_1 \nu_2; \omega_1 \omega_2} \equiv \mathcal{F}[S_{t_1 t_2; t'_1 t'_2}] = \delta(\nu_1 - \omega_1)\delta(\nu_2 - \omega_2) + \delta(\nu_1 - \omega_2)\delta(\nu_2 - \omega_1) - \kappa_{ae}G(\nu_1; \omega_1)\delta(\nu_2 - \omega_2) - \kappa_{ae}G(\nu_2; \omega_2)\delta(\nu_1 - \omega_1) - \kappa_{ae}G(\nu_1; \omega_2)\delta(\nu_2 - \omega_1) - \kappa_{ae}G(\nu_2; \omega_1)\delta(\nu_1 - \omega_2) + \kappa_{ae}^2G(\nu_1, \nu_2; \omega_1, \omega_2), \quad (\text{S4})$$

where $G(\nu_1; \omega_1)$ and $G(\nu_1, \nu_2; \omega_1, \omega_2)$ are the Fourier transform of the corresponding time-domain Green's functions.

The frequency-domain Green's function can be computed using Feynman diagrams. In essence, the n -point Green's function is calculated using all connected Feynman diagrams with n external points, which are constructed from basic elements including the “propagator” and “vertex”. The propagator is the two-point free-particle Green's function and the vertex corresponds to the bare interaction. The Feynman diagram rules for the $\chi^{(2)}$ cavity are given below:

- Propagator: $\frac{i}{\omega - \alpha_{a(b)}}$, where $\alpha_{a(b)} \equiv \omega_{a(b)} - i\frac{\kappa_{a(b)}}{2}$,
- Vertex: $-ig$,
- Impose energy conservation at each vertex: $\frac{1}{\sqrt{2\pi}}\delta(\sum \omega - \sum \nu)$,
- Integrate undetermined momentum: $\int d\omega \int d\nu$.
- Multiply the symmetry factor: $m!$ for m propagators of the same mode connecting two vertices or connecting a vertex with m external points.

The Feynman diagrams corresponding to the propagator and vertex are shown in Fig. S1a.

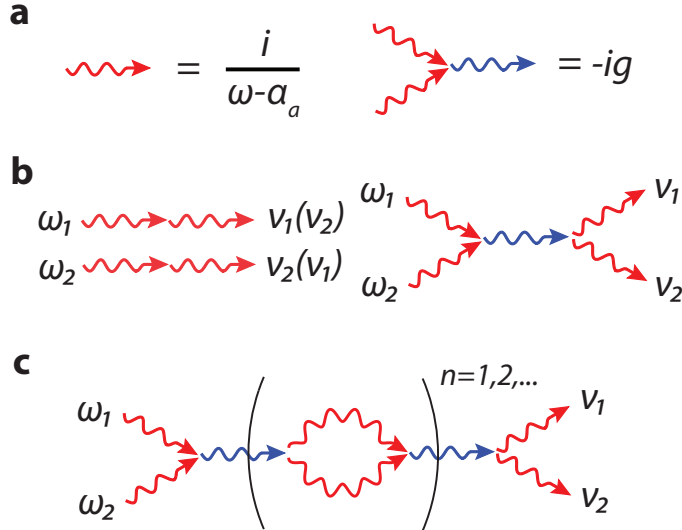


FIG. S1. **a**. Propagator and vertex of $\chi^{(2)}$ interaction. **b** Leading-order Feynman diagrams for two-photon scattering. **c** Higher-order Feynman diagrams involved in two-photon scattering. The part in the bracket is repeated for n times, $n \geq 1$.

The two-point Green's function (to the leading order) thus is

$$G(\nu_1; \omega_1) = \frac{i}{\omega_1 - \alpha_a} \delta(\nu_1 - \omega_1). \quad (\text{S5})$$

As a result, according to Eq. S3, we have

$$S_{\nu_1; \omega_1} = \left[1 - \frac{i\kappa_{ae}}{\omega_1 - \alpha_a} \right] \delta(\nu_1 - \omega_1) \equiv t_{\omega_1} \delta(\nu_1 - \omega_1), \quad (\text{S6})$$

where t_{ω_1} is the single-photon transmission coefficient.

Fig. S1b shows the leading-order Feynman diagrams that contribute to the four-point Green's function. The first diagram is the uncorrelated transport of the two photons. The second diagram, representing the virtual photon-mediated scattering, is calculated following the Feynman diagram rule as:

$$\begin{aligned} & (2!)^2 \frac{i}{\omega_1 - \alpha_a} \frac{i}{\omega_2 - \alpha_a} \frac{-ig}{\sqrt{2\pi}} \int dq \delta(q - \omega_1 - \omega_2) \frac{i}{q - \alpha_b} \frac{-ig}{\sqrt{2\pi}} \delta(q - \nu_1 - \nu_2) \frac{i}{\nu_1 - \alpha_a} \frac{i}{\nu_2 - \alpha_a} \\ & = -\frac{2ig^2}{\pi} \frac{1}{(\omega_1 - \alpha_a)(\omega_2 - \alpha_a)(\nu_1 - \alpha_a)(\nu_2 - \alpha_a)(\omega_1 + \omega_2 - \alpha_b)} \delta(\nu_1 + \nu_2 - \omega_1 - \omega_2). \end{aligned} \quad (\text{S7})$$

Thus, the four-point Green's function and two-photon scattering matrix are found to be

$$\begin{aligned} G(\nu_1, \nu_2; \omega_1, \omega_2) & = -\frac{1}{(\omega_1 - \alpha_a)(\omega_2 - \alpha_a)} [\delta(\nu_1 - \omega_1)\delta(\nu_2 - \omega_2) + \delta(\nu_1 - \omega_2)\delta(\nu_2 - \omega_1)] \\ & - \frac{2ig^2}{\pi} \frac{1}{(\omega_1 - \alpha_a)(\omega_2 - \alpha_a)(\nu_1 - \alpha_a)(\nu_2 - \alpha_a)(\omega_1 + \omega_2 - \alpha_b)} \delta(\nu_1 + \nu_2 - \omega_1 - \omega_2) \end{aligned} \quad (\text{S8})$$

and

$$\begin{aligned} S_{\nu_1 \nu_2; \omega_1 \omega_2} & = t_{\omega_1} t_{\omega_2} [\delta(\nu_1 - \omega_1)\delta(\nu_2 - \omega_2) + \delta(\nu_1 - \omega_2)\delta(\nu_2 - \omega_1)] \\ & - \frac{2ig^2}{\pi} \frac{\kappa_{ae}^2}{(\omega_1 - \alpha_a)(\omega_2 - \alpha_a)(\nu_1 - \alpha_a)(\nu_2 - \alpha_a)(\omega_1 + \omega_2 - \alpha_b)} \delta(\nu_1 + \nu_2 - \omega_1 - \omega_2), \end{aligned} \quad (\text{S9})$$

respectively.

The exact expression of the S -matrix can be obtained by including all higher-order Feynman diagrams as shown

in Fig. S1c, which yields

$$S_{\nu_1 \nu_2; \omega_1 \omega_2} = t_{\omega_1} t_{\omega_2} [\delta(\nu_1 - \omega_1) \delta(\nu_2 - \omega_2) + \delta(\nu_1 - \omega_2) \delta(\nu_2 - \omega_1)] - \kappa_{ae}^2 \frac{2ig^2}{\pi} \frac{\omega_1 + \omega_2 - 2\alpha_a}{(\omega_1 - \alpha_a)(\omega_2 - \alpha_a)(\nu_1 - \alpha_a)(\nu_2 - \alpha_a)(\omega_1 + \omega_2 - \lambda_1)(\omega_1 + \omega_2 - \lambda_2)} \delta(\nu_1 + \nu_2 - \omega_1 - \omega_2), \quad (\text{S10})$$

where $\lambda_{1,2} = \frac{1}{2}(2\alpha_a + \alpha_b) \pm \frac{1}{2}\sqrt{(2\alpha_a - \alpha_b)^2 + 8g^2}$ are the eigenfrequencies of the closed Hilbert space of $\{|2_a 0_b\rangle, |0_a 1_b\rangle\}$ in the presence of interaction $H_{\text{int}} = \hbar g(a^\dagger b + a b^\dagger)$. It can be straightforwardly verified that Eq. S9 contains the leading-order terms up to $O(g^2/\kappa^2)$ of Eq. S10.

The result of the S -matrix here applies to generic waveguide-coupled cavity systems, where t_ω may not take the form of Eq. S6 but depends on the specific construction of the photonic circuit.

B. Second-order correlation function

Here we calculate the second-order correlation function of the transported photons via the $\chi^{(2)}$ nonlinear circuit for a weak coherent state input

$$|\psi_{\text{in}}\rangle = |0\rangle + \alpha |1_t\rangle + \frac{\alpha^2}{\sqrt{2}} |1_t 1_t\rangle + O(\alpha^3), \quad (\text{S11})$$

where α is the amplitude of the coherent state and $|1_t\rangle = |1\rangle e^{-i\omega t}$ represents a monochromatic single-photon state with frequency ω in the time domain. The second-order correlation function of the transported photons is given by

$$g^{(2)}(\tau) = \frac{\langle \psi_{\text{in}} | a_{\text{out}}^\dagger(t) a_{\text{out}}^\dagger(t + \tau) a_{\text{out}}(t + \tau) a_{\text{out}}(t) | \psi_{\text{in}} \rangle}{|\langle \psi_{\text{in}} | a_{\text{out}}^\dagger(t) a_{\text{out}}(t) | \psi_{\text{in}} \rangle|^2}. \quad (\text{S12})$$

Using Eq. S11 and keeping the leading order terms in $|\psi_{\text{in}}\rangle$, we have

$$\begin{aligned} & \langle \psi_{\text{in}} | a_{\text{out}}^\dagger(t) a_{\text{out}}(t) | \psi_{\text{in}} \rangle \\ &= |\alpha|^2 \langle 1_t | a_{\text{out}}^\dagger(t) a_{\text{out}}(t) | 1_t \rangle \\ &= |\alpha|^2 \langle 1_t | a_{\text{out}}^\dagger(t) | 0 \rangle \langle 0 | a_{\text{out}}(t) | 1_t \rangle \\ &= |\alpha|^2 \int d\nu e^{i\nu t} \langle 1_\omega | a_{\text{out}}^\dagger(\nu) | 0 \rangle \int d\tilde{\nu} e^{-i\tilde{\nu} t} \langle 0 | a_{\text{out}}(\tilde{\nu}) | 1_\omega \rangle \\ &= |\alpha|^2 \int d\nu e^{i\nu t} S_{\nu; \omega}^* \int d\tilde{\nu} e^{-i\tilde{\nu} t} S_{\tilde{\nu}; \omega} \\ &= |\alpha|^2 |t_\omega|^2 \end{aligned} \quad (\text{S13})$$

and

$$\begin{aligned} & \langle \psi_{\text{in}} | a_{\text{out}}^\dagger(t) a_{\text{out}}^\dagger(t + \tau) a_{\text{out}}(t + \tau) a_{\text{out}}(t) | \psi_{\text{in}} \rangle \\ &= \frac{|\alpha|^4}{2} \langle 1_t 1_t | a_{\text{out}}^\dagger(t) a_{\text{out}}^\dagger(t + \tau) a_{\text{out}}(t + \tau) a_{\text{out}, 1}(t) | 1_t 1_t \rangle \\ &= \frac{|\alpha|^4}{2} \int d\nu_1 d\nu_2 \langle 1_\omega 1_\omega | a_{\text{out}}^\dagger(\nu_1) a_{\text{out}}^\dagger(\nu_2) | 0 \rangle e^{i\nu_1 t + i\nu_2(t + \tau)} \\ & \quad \times \int d\tilde{\nu}_1 d\tilde{\nu}_2 \langle 0 | a_{\text{out}}(\tilde{\nu}_2) a_{\text{out}}(\tilde{\nu}_1) | 1_\omega 1_\omega \rangle e^{-i\tilde{\nu}_1 t - i\tilde{\nu}_2(t + \tau)} \\ &= \frac{|\alpha|^4}{4} \int d\nu_1 d\nu_2 S_{\nu_1 \nu_2; \omega \omega}^* e^{i\nu_1 t + i\nu_2(t + \tau)} \\ & \quad \times \int d\tilde{\nu}_1 d\tilde{\nu}_2 S_{\tilde{\nu}_1 \tilde{\nu}_2; \omega \omega} e^{-i\tilde{\nu}_1 t - i\tilde{\nu}_2(t + \tau)} \\ &= |\alpha|^4 |t_\omega^2 + T(\omega, \tau)|^2, \end{aligned} \quad (\text{S14})$$

where the S -matrices are given by Eqs. S6 and S9 and

$$T(\omega, \tau) = -\frac{g^2 \kappa_{ae}^2}{(2\omega - \alpha_b)(\omega - \alpha_a)^3} e^{-i|\tau|(\alpha_a - \omega)}. \quad (\text{S15})$$

As a result, we have

$$g^{(2)}(\tau) = \frac{|t_\omega^2 + T(\omega, \tau)|^2}{|t_\omega^2|^2}. \quad (\text{S16})$$

C. Modeling of the effective one-port photonic circuit

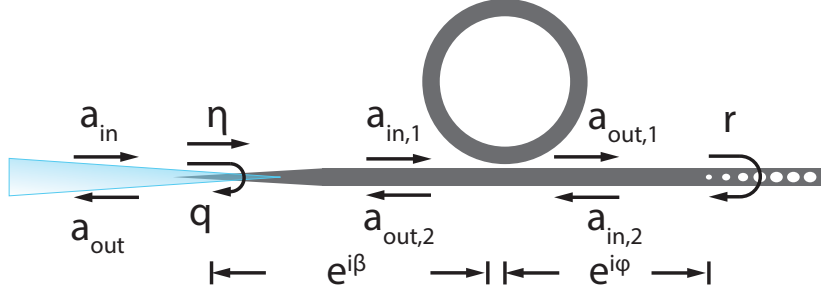


FIG. S2. Input-output relation of the effective one-port photonic circuit.

For an ideal ring resonator, the clockwise (CW) and counterclockwise (CCW) resonances are degenerate with frequency ω_0 . For the fabricated high-index InGaP ring resonator, the CW and CCW resonances couple due to the surface roughness induced back-scattering. As illustrated in Fig. S2, the input-output equation for the CW and CCW resonances is given by

$$\frac{d}{dt} \begin{pmatrix} a_{\text{cw}} \\ a_{\text{ccw}} \end{pmatrix} = -i \begin{pmatrix} \omega_0 - i\frac{\kappa_{\text{cw}}}{2} & V \\ V & \omega_0 - i\frac{\kappa_{\text{ccw}}}{2} \end{pmatrix} \begin{pmatrix} a_{\text{cw}} \\ a_{\text{ccw}} \end{pmatrix} + \begin{pmatrix} 0 & \sqrt{\kappa_{\text{cw},e}} \\ \sqrt{\kappa_{\text{ccw},e}} & 0 \end{pmatrix} \begin{pmatrix} a_{\text{in},1} \\ a_{\text{in},2} \end{pmatrix}, \quad (\text{S17})$$

$$\begin{pmatrix} a_{\text{out},1} \\ a_{\text{out},2} \end{pmatrix} = \begin{pmatrix} a_{\text{in},1} \\ a_{\text{in},2} \end{pmatrix} - \begin{pmatrix} 0 & \sqrt{\kappa_{\text{ccw},e}} \\ \sqrt{\kappa_{\text{cw},e}} & 0 \end{pmatrix} \begin{pmatrix} a_{\text{cw}} \\ a_{\text{ccw}} \end{pmatrix}, \quad (\text{S18})$$

where $\kappa_{\text{cw(ccw)}} = \kappa_{\text{cw(ccw),e}} + \kappa_{\text{cw(ccw),i}}$ and V is the coupling between the CW and CCW resonances.

The photonic crystal mirror with non-unity reflection acts like a beamsplitter, which relates $a_{\text{out},1}$ and $a_{\text{in},2}$ by

$$a_{\text{in},2} = e^{i\varphi} (ire^{i\varphi} a_{\text{out},1} + ta_n), \quad (\text{S19})$$

where φ is the waveguide phase between the ring and the photonic crystal mirror, r and t are the real reflection and transmission coefficient of the photonic crystal mirror, and a_n represents the noise operator.

By eliminating $a_{\text{out},1}$ and $a_{\text{in},2}$ from Eqs. S17-S19, we obtain

$$\frac{d}{dt} \begin{pmatrix} a_{\text{cw}} \\ a_{\text{ccw}} \end{pmatrix} = -i \begin{pmatrix} \omega_0 - i\frac{\kappa_{\text{cw}}}{2} & V + \sqrt{\kappa_{\text{cw},e} \kappa_{\text{ccw},e}} re^{i2\varphi} \\ V & \omega_0 - i\frac{\kappa_{\text{ccw}}}{2} \end{pmatrix} \begin{pmatrix} a_{\text{cw}} \\ a_{\text{ccw}} \end{pmatrix} + \begin{pmatrix} i\sqrt{\kappa_{\text{cw},e}} re^{i2\varphi} \\ \sqrt{\kappa_{\text{ccw},e}} \end{pmatrix} a_{\text{in},1} + \begin{pmatrix} \sqrt{\kappa_{\text{cw},e}} te^{i\varphi} \\ 0 \end{pmatrix} a_n, \quad (\text{S20})$$

$$a_{\text{out},2} = ire^{i2\varphi} a_{\text{in},1} - \sqrt{\kappa_{\text{cw},e}} a_{\text{cw}} - i\sqrt{\kappa_{\text{ccw},e}} re^{i2\varphi} a_{\text{ccw}} + te^{i\varphi} a_n. \quad (\text{S21})$$

From now on, we assume the CW and CCW resonances have the same dissipation rate and omit the label. To obtain the reflection coefficient of the device, we solve Eqs. S20 and S21 in the frequency domain by ignoring the noise

operator, which yields

$$a_{\text{out},2}[\omega] = i \left[r e^{i2\varphi} - \kappa_e \begin{pmatrix} 1 & i r e^{i2\varphi} \end{pmatrix} \begin{pmatrix} \omega - \omega_0 + i \frac{\kappa}{2} & -V - \kappa_e r e^{i2\varphi} \\ -V & \omega - \omega_0 + i \frac{\kappa}{2} \end{pmatrix}^{-1} \begin{pmatrix} i r e^{i2\varphi} \\ 1 \end{pmatrix} \right] a_{\text{in},1}[\omega]. \quad (\text{S22})$$

The reflection is zero (i.e., $a_{\text{out},2}[\omega] = 0$) when

$$\left(\cos 2\varphi + \frac{r \Delta \kappa^2}{2V \kappa_e} \right)^2 = 1 - \frac{r^2 \Delta \kappa^2}{\kappa_e^2} \quad (\text{S23})$$

and

$$\begin{aligned} \omega &= \omega_0 \pm \sqrt{V^2 + \Delta \kappa^2 + V(\kappa_e/r) \cos 2\varphi} \\ &= \omega_0 \pm \sqrt{V^2 + (\Delta \kappa/2)^2 \pm V \sqrt{(\kappa_e/r)^2 - \Delta \kappa^2}}, \end{aligned} \quad (\text{S24})$$

where $\Delta \kappa = \kappa_i - \kappa_e$. It is obvious that the frequency corresponding to the zero reflection is not the bare cavity resonance frequency.

From now on, we consider the large splitting limit, i.e., $V \gg \kappa$, to simplify the two-mode modeling. By eliminating $a_{\text{out},1}$ and $a_{\text{in},2}$ from Eqs.S17-S19, and diagonalizing Eq. S17, we obtain

$$\frac{d}{dt} \begin{pmatrix} a_e \\ a_o \end{pmatrix} = -i \begin{pmatrix} \omega_e - i \frac{\kappa_e}{2} & \\ & \omega_o - i \frac{\kappa_o}{2} \end{pmatrix} \begin{pmatrix} a_e \\ a_o \end{pmatrix} + \frac{1}{\sqrt{2}} \begin{pmatrix} i \sqrt{\kappa_e} r e^{i2\varphi} + \sqrt{\kappa_e} \\ i \sqrt{\kappa_e} r e^{i2\varphi} - \sqrt{\kappa_e} \end{pmatrix} a_{\text{in},1} + \frac{1}{\sqrt{2}} \begin{pmatrix} \sqrt{\kappa_e} t e^{i\varphi} \\ \sqrt{\kappa_e} t e^{i\varphi} \end{pmatrix} a_n, \quad (\text{S25})$$

$$a_{\text{out},2} = i r e^{i2\varphi} a_{\text{in},1} - \frac{1}{\sqrt{2}} (i \sqrt{\kappa_e} r e^{i2\varphi} + \sqrt{\kappa_e}) a_e - \frac{1}{\sqrt{2}} (-i \sqrt{\kappa_e} r e^{i2\varphi} + \sqrt{\kappa_e}) a_o + t e^{i\varphi} a_n, \quad (\text{S26})$$

where $a_{e(o)} = \frac{1}{\sqrt{2}} (a_{\text{cw}} \pm a_{\text{ccw}})$, $\kappa_{e(o)} = \kappa \mp r \kappa_e \sin 2\varphi$, and

$$\omega_{e(o)} = \omega_0 \pm (V + \frac{1}{2} r \kappa_e \cos 2\varphi). \quad (\text{S27})$$

As a result, in the large splitting limit, the hybridized even and odd modes, a_e and a_o , become independently described by the input-output equations

$$\frac{da_{o(e)}}{dt} = -i(\omega_{o(e)} - i \frac{\kappa_{o(e)}}{2}) a_{o(e)} - \frac{\sqrt{\kappa_e} (\pm 1 - i r e^{i2\varphi})}{\sqrt{2}} a_{\text{in},1}, \quad (\text{S28})$$

$$a_{\text{out},2} = i r e^{i2\varphi} a_{\text{in},1} - \frac{\sqrt{\kappa_e} (1 \mp i r e^{i2\varphi})}{\sqrt{2}} a_{o(e)}. \quad (\text{S29})$$

Replacing $\frac{\sqrt{\kappa_e} (1 \mp i r e^{i2\varphi})}{\sqrt{2}}$ with $\sqrt{\kappa_{(o)e,e}} e^{i(\theta + \pi/4)}$, $a_{o(e)} e^{-i(\theta - \pi/4)}$ with $a_{o(e)}$, and $a_{\text{out},2} e^{-2i(\theta - \pi/4)}$ with a_{out} , the input-output relations are simplified to

$$\frac{da_{o(e)}}{dt} = -i(\omega_{o(e)} - i \frac{\kappa_{o(e)}}{2}) a_{o(e)} - i \sqrt{\kappa_{o(e),e}} a_{\text{in},1}, \quad (\text{S30})$$

$$a_{\text{out},2} = R a_{\text{in},1} - i \sqrt{\kappa_{o(e),e}} a_{o(e)}, \quad (\text{S31})$$

where

$$R = -r e^{i(2\varphi - 2\theta)} \quad (\text{S32})$$

and the effective external and intrinsic dissipation rates of $a_{o(e)}$ are

$$\kappa_{e(o),e} = \kappa_e \left(\frac{1+r^2}{2} \mp r \sin 2\varphi \right) \quad (\text{S33})$$

and

$$\kappa_{e(o),i} = \kappa_i + \frac{t^2}{2} \kappa_e. \quad (\text{S34})$$

After Fourier transform, the input-output relation in the frequency domain is obtained

$$\begin{aligned} a_{\text{out},2}[\omega] &= \left[R - \frac{i\kappa_{o(e),e}}{\omega - \omega_{o(e)} + i\kappa_{o(e)}/2} \right] a_{\text{in},1}[\omega] \\ &\equiv \tilde{t}_\omega a_{\text{in},1}[\omega]. \end{aligned} \quad (\text{S35})$$

The zero-reflection condition at the large splitting limit is

$$\sin 2\varphi = \pm \frac{r\Delta\kappa}{\kappa_e} \quad (\text{S36})$$

and

$$\begin{aligned} \omega &= \omega_0 \pm \left(V + \frac{1}{2} \frac{\kappa_e}{r} \cos 2\varphi \right) \\ &= \omega_0 \pm \left(V \pm \frac{1}{2} \sqrt{(\kappa_e/r)^2 - \Delta\kappa^2} \right), \end{aligned} \quad (\text{S37})$$

which is consistent with Eqs. S23 and S24. From Eq. S36, it is seen that the zero-reflection condition can be achieved only if $\kappa_i \leq (1 + \frac{1}{r})\kappa_e$. Note Eq. S36 is not the same as $\kappa_{e(o),e} = \kappa_{e(o),i}$ for $r < 1$ because of the Fano interference. The difference between Eqs. S37 and S27 gives the local minimum transmission-cavity resonance detuning in the large-splitting limit.

Next, we derive the fiber-to-fiber transmission of the signal, taking into account of the direct reflection at the fiber-coupler region. The transmission relation of the fiber coupler can be modeled as

$$a_{\text{out}} = iqa_{\text{in}} + e^{i\beta} \eta a_{\text{out},2}, \quad (\text{S38})$$

$$a_{\text{in},1} = e^{i\beta} \eta a_{\text{in}}. \quad (\text{S39})$$

Therefore,

$$\begin{aligned} a_{\text{out}}[\omega] &= \left[\eta^2 e^{2i\beta} \left(R - \frac{i\kappa_{o(e),e}}{\omega - \omega_{o(e)} + i\kappa_{o(e)}/2} \right) + iq \right] a_{\text{in}}[\omega] \\ &\equiv t_\omega a_{\text{in}}[\omega]. \end{aligned} \quad (\text{S40})$$

The second-order correlation function, following the derivation in Section IA, is given by

$$\begin{aligned} g^{(2)}(\tau) &= \frac{|t_\omega^2 + \eta^4 e^{4i\beta} T(\omega, \tau)|^2}{|t_\omega^2|^2} \\ &= \frac{|(R + iq\eta^{-2} e^{-2i\beta})^2 \bar{t}_\omega^2 + T(\omega, \tau)|^2}{|(R + iq\eta^{-2} e^{-2i\beta})^2 \bar{t}_\omega^2|^2}, \end{aligned} \quad (\text{S41})$$

where

$$\bar{t}_\omega = 1 - \frac{1}{R + iq\eta^{-2} e^{-2i\beta}} \frac{i\kappa_{o(e),e}}{\omega - \omega_{o(e)} + i\kappa_{o(e)}/2} \quad (\text{S42})$$

is the transmission coefficient normalized to the off-resonance background, i.e., the one that is measured and quoted throughout this paper. $T(\omega, \tau)$ is calculated using Eq. S15 (note $\omega \equiv k$) with the effective dissipation rate given by

Eqs. S33 and S36.

If $q \ll |R|\eta^2$, which is satisfied for our devices (see Table S1),

$$\begin{aligned} g^{(2)}(\tau) &\approx \frac{|R^2 \tilde{t}_\omega^2 + T(\omega, \tau)|^2}{|R^2 \tilde{t}_\omega^2|^2} \\ &\approx \frac{|\tilde{t}_\omega^2 + T(\omega, \tau)|^2}{|\tilde{t}_\omega^2|^2}, \end{aligned} \quad (\text{S43})$$

where \tilde{t}_ω is given by Eq. S35.

In general, for the split resonances, the local minimum of the transmission spectrum is detuned from the bare cavity frequency. Thus, when the signal is at the local minimum of the transmission, this detuning induces an oscillation of $T(\omega, \tau)$ (Eq. S15), which is the cause of the repulsive photon-photon interaction.

II. DEVICE FABRICATION

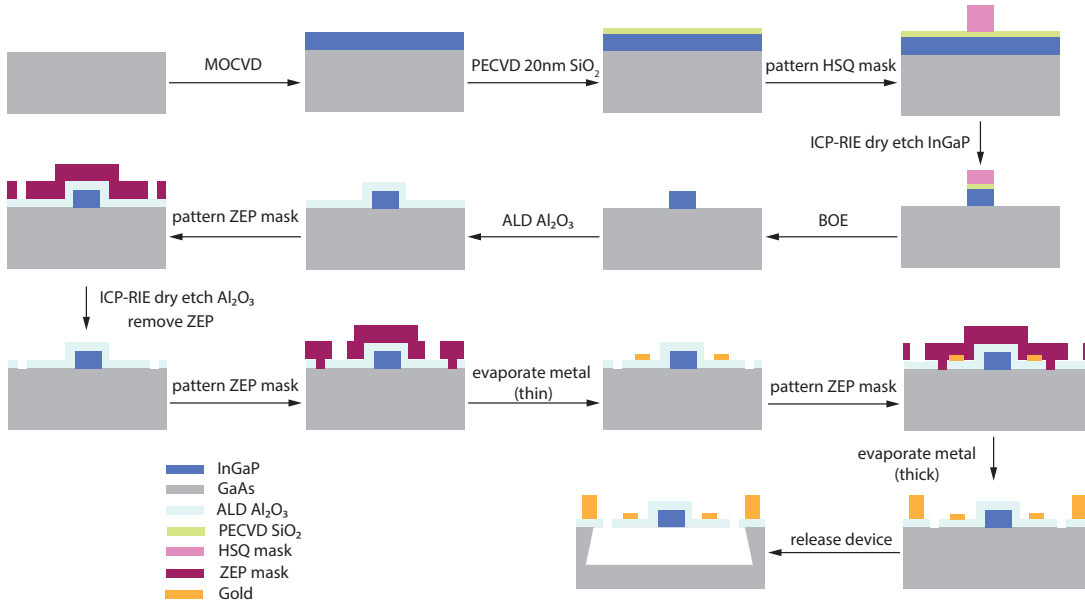


FIG. S3. Fabrication process of the InGaP photonic circuit.

Fig. S3 shows the flow chart of the fabrication process of the InGaP photonic circuit. The devices are fabricated from the 115 nm thick disordered $\text{In}_{0.48}\text{Ga}_{0.52}\text{P}$ thin film grown on GaAs substrate by metal-organic chemical vapor deposition ($T = 545$ C, $\text{V}/\text{III} = 48$, precursors: trimethylindium, trimethylgallium and PH_3). The device pattern is defined using a 150 keV electron beam lithography tool and 150 nm thick negative tone resist hydrogen silsesquioxane (HSQ). A 20 nm thick layer of silicon dioxide is deposited on InGaP via plasma-enhanced chemical vapor deposition (PECVD) to promote the adhesion of HSQ. The device pattern is transferred to InGaP layer via inductively coupled plasma reactive-ion etch (ICP-RIE) using a mixture of $\text{Cl}_2/\text{CH}_4/\text{Ar}$ gas with a selectivity of InGaP: HSQ: PECVD $\text{SiO}_2 = 240: 90: 80$. After a short buffered oxide etch to remove the residual oxide (both HSQ and PECVD oxide), a layer of 35 nm thick aluminum oxide is deposited on the chip via atomic layer deposition (ALD). This layer will serve as the mechanical support for the suspended device. A second electron beam lithography and subsequent ICP-RIE using CHF_3 gas are applied to pattern etch-through holes in the aluminum oxide layer for the undercut of the InGaP device. Next, a third electron beam lithography followed by electron-beam evaporation of 5 nm thick chromium and 20 nm thick gold is performed to define the high-resistance wires next to the 1550-nm light waveguide as the phase shifter. Then, a fourth electron beam lithography followed by electron-beam evaporation of 10 nm thick chromium and 150 nm thick gold is used to define the low-resistance large metal pads that connect several devices in parallel. In this way, the resistive heating is concentrated at the phase shifter without heating up the whole chip. Finally, the InGaP device is released from the GaAs substrate using citric acid-based selective etching. The suspended InGaP

device is mechanically anchored to the aluminum oxide membrane.

III. THE INGAP PHOTONIC CIRCUIT: DESIGN AND CHARACTERIZATION

Fig. 2a shows scanning electron microscopy (SEM) images of the fabricated photonic circuit. The design of the phase-matched microring resonator follows Ref. [3]. The nominal ring radius is 5 μm . The microring resonator is coupled to two bus waveguides for transmitting the 1550-nm and 775-nm wavelength light, respectively. The 1550-nm band waveguide is 750 nm wide in the ring-waveguide coupled region and is separated from the ring by 350 nm. It decouples from the 775-nm TM_{00} microring resonance because of the tight field confinement of the latter and the large ring-waveguide gap. On the other hand, the 775-nm wavelength pulley waveguide is 280 nm wide with a wrap angle of 6 degrees and a ring-waveguide gap of 250 nm. It decouples from the 1550-nm TE_{00} microring resonance because of the significantly different mode index of the 1550-nm TE_{00} mode in the narrow waveguide and the wide microring. Both bus waveguides are terminated with a photonic crystal mirror that is designed to reflect the 1550-nm TE and 775-nm TM light, respectively. At the end of the 1550-nm light waveguide, a section of 100- μm -long metal wire is fabricated on both sides of the waveguide in order to tune the phase of the waveguide via resistive heating and thermo-optic effect. The metal wires are 2 μm wide, 25 nm thick, and separated from the waveguide by 800 nm. The two bus waveguides are joined at a 1550-nm/775-nm wavelength-division multiplexer (WDM) which adiabatically couples the 1550-nm light between the two adjacent waveguides while forbidding the coupling of 775-nm light. One waveguide of the WDM is then connected to a tapered fiber-optic coupler which couples both 1550-nm TE polarized and 775-nm TM polarized light from a tapered fiber into the photonic circuit with an efficiency of about 60% and 20%, respectively. The other waveguide of the WDM is tapered down to a width of 30 nm to reduce reflection from the waveguide end. An array of microrings with the width swept at 1 nm step are fabricated to achieve phase- and frequency-matched resonators. We also group 50 microrings in one device which effectively enhances the probability to realize the matching condition of a device and simplifies the measurement. The devices are electronically wired in parallel and can be tuned by a DC voltage. Fig. S4a shows the measured 1550-nm band reflection spectrum of a device.

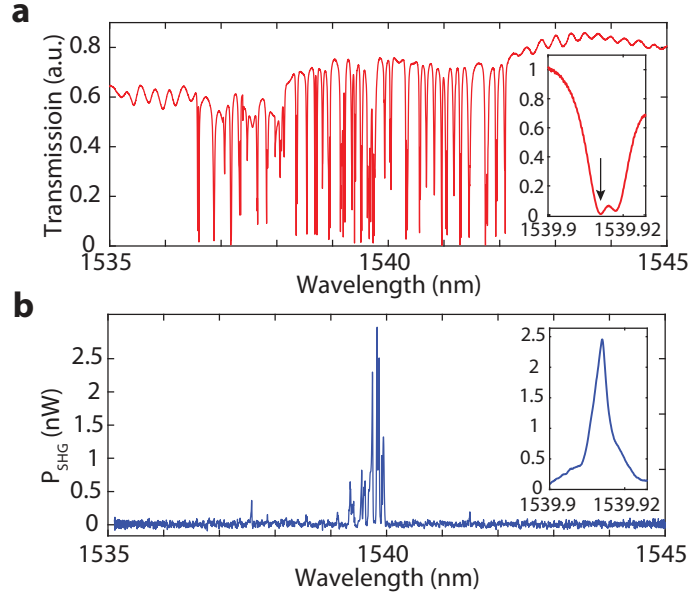


FIG. S4. **a.** 1550-nm band TE spectrum. Inset is the normalized spectrum of the phase- and frequency-matched resonance (arrow) used in the experiment. **b.** Second-harmonic power spectrum corresponding to the input pump wavelength (signal difference between the wide scan and the inset is due to the wavelength resolution of wide scan).

To characterize the fiber coupling efficiency, we fabricated on the same chip a simple waveguide device that has two identical waveguide couplers at the two ends and measured the transmission efficiency η_t to obtain the one-way coupling efficiency $\eta_{a(b),c} = \sqrt{\eta_{a(b),t}} = 60\%$ and 20% for 1550-nm band TE and 775-nm band TM light, respectively. We also fabricated a waveguide device that has the same waveguide coupler on one end and a photonic crystal mirror on the other end. By measuring the reflection efficiency, and together with the measured coupler efficiency, we can get

the mirror reflection efficiency $\eta_{a(b),m} = 90\%$ and 2% for 1550-nm band TE and 775-nm band TM light, respectively. Then, we measure the total reflection coefficient η for the actual device used in the experiment, $\eta = \eta_c^2 \cdot \eta_{\text{WDM}}^2 \cdot \eta_m$, where η_{WDM} is the transmission efficiency of the on-chip WDM. By this, $\eta_{a(b),\text{WDM}}$ are found to be 90% and 98%, respectively. After the tapered fiber tip is glued to the device, $\eta_{a(b),c}$ drops due to the higher refractive index of the adhesive than that of the fiber. By measuring the change in the total reflection coefficient of the device, we find the coupler efficiency drops to 29% and 1.2% for 1550-nm band TE and 775-nm band TM light, respectively.

The nonlinear mode coupling of the phase-matched microring resonator is characterized using SHG (see Section VII). Fig. S4b shows the SHG power spectrum of the device. Table S1 summarizes the key parameters for a typical phase- and frequency-matched device.

TABLE S1. Summary of measured device parameters.

Nonlinear mode interaction ($g/2\pi$)	6.5 MHz
1550-nm resonance intrinsic quality factor (Q_{ai})	2.5×10^5
775-nm resonance intrinsic quality factor (Q_{bi})	5.1×10^4
775-nm resonance external quality factor (Q_{be})	2.0×10^6
1550-nm TE photonic crystal mirror reflection	90%
775-nm TM photonic crystal mirror reflection	2%
Fiber coupler efficiency for 1550-nm TE	before glue: 60%; after glue: 29%
Fiber coupler efficiency for 775-nm TM	before glue: 20%; after glue: 1.2%
Fiber coupler direct reflection for 1550-nm light	-30 dB
WDM efficiency for 1550-nm TE	90%
WDM efficiency for 775-nm TM	98%

A. On-chip wavelength-division multiplexer

An on-chip WDM is used to (de)multiplex the 1550-nm and 775-nm band light, which are transmitted via individual waveguides for optimal coupling with the microring resonator. The on-chip WDM also enables the use of a single fiber-optic coupler for coupling of both 1550-nm and 775-nm band light between the optical fiber and the device.

The WDM consists of two adiabatically tapered waveguides in parallel. The gap between the two waveguides is sufficiently large such that the 775-nm-band TM_{00} mode does not couple between the two waveguides. The input and coupling waveguide is adiabatically tapered down (from 430 nm to 290 nm over a length of 100 μm) and up (from 290 nm to 430 nm), respectively, such that the 1550-nm-band TE_{00} light couples between the two adjacent waveguides with a high efficiency $> 90\%$. Fig. S5 shows the finite-difference time-domain (FDTD) simulation of the transmission of the 1550-nm-band TE_{00} light and 775-nm-band TM_{00} light through the WDM.

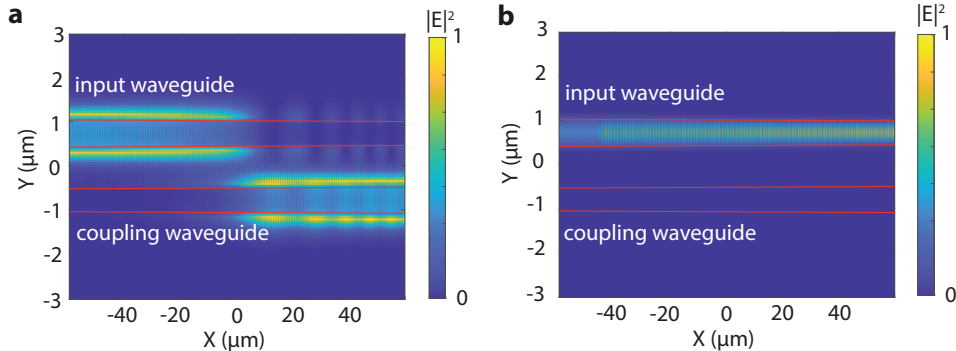


FIG. S5. FDTD simulation of propagation of 1550-nm TE_{00} light (a) and 775-nm TM_{00} light (b) in the WDM.

B. Resistive phase shifter

A resistive heater is used to tune the waveguide phase. The phase change in the tuning section of the waveguide caused by the temperature change is given by

$$\Delta\phi = \Delta n \frac{\omega}{c} L = \frac{dn}{dT} \Delta T \frac{\omega}{c} L \quad (\text{S44})$$

where L is the waveguide length and $\frac{dn}{dT}$ is the thermo-optic coefficient.

In the device, the resistive heater is made from gold wires that are 100 μm long on both sides of the waveguide, 2 μm wide, 25 nm thick, and separated from the waveguide by 800 nm. Fig. S6a shows the temperature distribution near the waveguide/heater for a voltage of 0.6 V. Thanks to the released structure of the thin-membrane device, the heat is concentrated locally around the waveguide. Fig. S6b shows the calculated waveguide phase change versus applied voltage based on the simulated temperature of the waveguide.

Although the simulation is performed using the room-temperature material parameters, it turns out that the performance of the phase shifter at 4 K is close to the simulation. We observed that the waveguide phase can be tuned by 2π for a voltage < 1 V. Some literatures report significant drop of thermo-optic coefficient of materials at cryogenic temperatures; e.g., Ref. [4] measured a four orders-of-magnitude reduction in bulk silicon substrate at 5 K compared to 300 K. Our measurement indicates that, however, the reduction of thermo-optic coefficient is likely to be mild and follows a similar reduction of thermal conductance for micro-/nano-structures in thin-film materials.

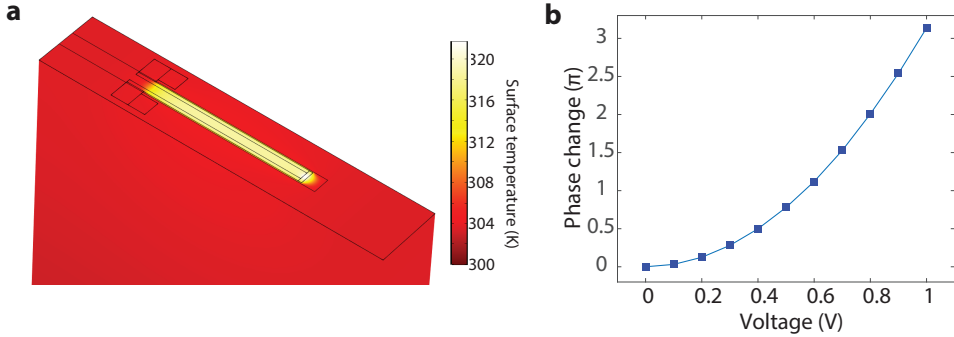


FIG. S6. a. Finite-element-method simulation of the temperature distribution around the release waveguide at 300 K for an applied voltage of 0.6 V. We used the room-temperature thermal-optic coefficient of InGaP, $2 \times 10^{-4} \text{ K}^{-1}$, and the room-temperature conductivity of gold, $4.517 \times 10^7 \text{ S/m}$, in the simulation. b. Calculated waveguide phase change based on the simulated waveguide temperature for applied voltages.

IV. EXPERIMENTAL SETUP

Fig. S7 shows a schematic plot of the experimental setup. Light from a tunable external cavity diode laser (New Focus TLB-6728) is filtered by an optical grating filter (JDS TB9223, 3 dB bandwidth 0.55 nm, 20 dB bandwidth 1.5 nm) and a fiber Febry-Perot (FP) filter (LUNA, 50 GHz free spectral range, 400 finesse) to eliminate the amplified spontaneous emission (ASE) and side-mode emission (at multiples of 2.4 GHz relative to the laser frequency) of the laser. One resonance of the FP filter is locked to the laser frequency via a dither feedback controller. The filtered light is then passed through a fiber polarizer (50 dB extinction) to eliminate unpolarized and orthogonally polarized light generated by random scattering in the fiber-optic circuit and, subsequently, a 1550-nm/775-nm WDM before coupling into the device. The WDM separates the 1550-nm and 775-nm (via second-harmonic generation) band light from the device. The 775-nm wavelength light is detected by an avalanche photodetector (Thorlabs APD440A). The 1550-nm wavelength light is further purified by a polarizer (40 dB extinction) and measured using the Hanbury-Brown and Twiss setup which consists of a 50:50 beamsplitter, two SNSPDs (Quantum Opus), and a time-correlated single-photon counting module (Time Tagger Ultra).

The device chip is wire-bonded to a printed circuit board for voltage tuning of the waveguide phase and is mounted in the mixing chamber of a dilution refrigerator (DR). The measurement, however, is performed at 4 K without condensation of the helium. A bare optical fiber is fed through the DR for transmitting the light. The tapered fiber

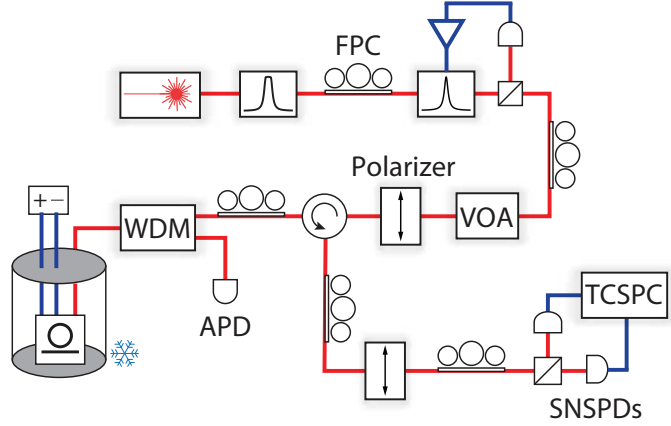


FIG. S7. **a.** Schematic of the experimental setup. FPC: fiber polarization controller. VOA: variable optical attenuator. WDM: wavelength-division multiplexer. APD: avalanche photodetector. SNSPDs: superconducting nanowire single-photon detector. TCSPC: time-correlated single-photon counting module.

tip is glued to the on-chip coupler for low-loss, mechanically-rigid fiber-optic coupling that is immune to the DR vibration (see Section VI).

V. NOISE SOURCES AND MITIGATION

A. Amplified spontaneous emission, laser side modes, and unpolarized light

In our experiment, tuning of the transmission of the photonic circuit near the critical-coupling regime relies on the destructive interference of light. Any incoherent light will lead to residual transmission which might obscure the signal. The major incoherent light sources in the experimental setup include the amplified spontaneous emission of the laser, laser side-mode emissions, and unpolarized light. To eliminate the broadband amplified spontaneous emission, we used a wavelength-tunable optical grating filter (JDS TB9223, 3 dB bandwidth 0.55 nm, 20 dB bandwidth 1.5 nm), which lowered the minimum normalized transmission from 2×10^{-3} to 1×10^{-4} at room temperature. We also used two polarizers (40 dB and 50 dB extinction ratio) to eliminate the unpolarized and random polarized light from the laser or generated through scattering in the optical fiber setup. At this level, the minimum transmission is limited by the thermomechanical and thermorefractive noises from the device (see below). To suppress these thermal noises, we placed the device chip in a dilution refrigerator but operated at 4 K. With the same setup, the minimum transmission is reduced to 1×10^{-5} , which is nevertheless higher than the residual thermal noise supposed to be at 4 K. We further used a narrow bandwidth fiber Fabry-Perot filter (LUNA, 50 GHz free spectral range, 400 finesse) to eliminate the laser side-mode emission at multiples of 2.4 GHz relative to the laser frequency as well as the residual ASE in the vicinity of the laser frequency. By doing so, the minimum transmission is reduced from 1×10^{-5} to 1×10^{-6} , which is dominated by the thermomechanical noise at 4 K.

B. Thermomechanical and thermorefractive noises

Besides the external incoherent light which causes residual transmission, the photonic device itself also generates noise photons upon incidence of the laser light. The InGaP photonic circuit is suspended with a thin Al_2O_3 membrane, which supports vibration modes with frequencies in the range of a few MHz to a few hundred MHz that couple to the microring resonator via the radiation-pressure force [5]. At finite temperatures, thermal motion of these vibration modes modulates the input light, generating Stokes and anti-Stokes (thermal) light, which cannot interfere with the input coherent signal. In addition, the phonon-scattered light has a super-Poissonian photon statistics with $g^{(2)}(0) > 1$. At room temperature and for the 5- μm -radius ring, the equivalent transmission corresponding to the thermomechanical noise is about 10^{-4} [5]. Thermomechanical noise is proportional to the phonon occupation and thus the temperature T .

Another source of thermal noise is the thermorefractive noise. The intrinsic fluctuation of the temperature in a finite

volume causes fluctuation of the refractive index, leading to jitter of the cavity frequency. The cavity frequency jitter effectively modulates the input light and generates noise photons. At room temperature and for the 5- μm -radius ring, the equivalent transmission corresponding to the thermorefractive noise is about 10^{-4} [5]. Thermorefractive noise has a quadratic dependence on the temperature ($\propto T^2$) [5, 6].

Since both thermal noises are temperature dependent, they can be suppressed at cryogenic temperatures. At 4 K, the equivalent transmission corresponding to the thermomechanical and thermorefractive noise is below 10^{-6} and 10^{-8} , respectively.

Table S2 summarizes major noise sources in our experiment and methods for mitigation.

TABLE S2. Summary of noise sources and methods of mitigation.

Noise	Mitigation	Before	After
Unpolarized light	Polarizer	3×10^{-3}	2×10^{-3}
ASE	Filter	2×10^{-3}	10^{-5}
Laser side mode	Filter	10^{-5}	$< 10^{-6}$
Thermomechanical noise	Cryogenic 4 K	10^{-4}	10^{-6}
Thermorefractive noise	Cryogenic 4 K	10^{-4}	10^{-8}

VI. CRYOGENIC NONLINEAR PHOTONICS EXPERIMENT

We outline the procedure of performing the nonlinear photonics experiment in a dilution refrigerator (DR), including identifying the phase-matched device and realizing mechanically-stable fiber-optic coupling which is particularly important for this experiment.

A. Frequency- and phase-matched device

Finding the frequency- and phase-matched device is achieved by scanning microrings with different width and measuring the SHG efficiency, as the phase-matched ring yields the greatest SHG efficiency. A tapered fiber is installed in the DR and the chip is mounted on a piezostage for scanning devices. The DR has an optical window which allows imaging and alignment of the device and tapered fiber. However, device scanning in the DR could be time-consuming. To mitigate this, we first perform the measurement in a room-temperature setup and identify the phase-matched device. Since the frequency shift of the 1550-nm and 775-nm band resonances from room temperature to 4 K is different, the phase-matched device at 4 K will be different from the one at room temperature. However, we find such a change, despite varying for each temperature cycle and each chip, is only a few devices corresponding to the change of ring width by a few nm. Fig. S8 shows the change of phase-matching ring width measured for several temperature cycles and change of the 1550-nm resonance wavelength of the phase-matched ring. To further simplify the measurement, we fabricated multiple microring resonators into a single device, so they can be measured altogether at once. Effectively, it enhances the probability for a single device to satisfy the phase- and frequency-matching condition. Such device arrangement also mitigates the possible cavity frequency discontinuity caused by the thickness nonuniformity of the device layer across large areas.

B. Mechanically-rigid fiber-optic coupler

Another challenge associated with the fiber-optic measurement in a DR is the vibration. The vibration of the DR causes relative movement between the tapered fiber and the chip even when they are in touch, leading to fluctuations of both the transmission and direct reflection of the fiber-optic coupler. Since the device is operated near the critical-coupling regime, signal transmission is sensitive to such fluctuations. To overcome this, after finding the phase-matched device at low temperature, we glue the tapered fiber to the device to make a mechanically-rigid fiber-optic coupling.

We first glued the tapered fiber tip to the tapered waveguide. We used a UV-cured, tack-free optical adhesive (Norland NOA 61, refractive index 1.56), as it allows a thin layer around the fiber tip and is 100% solid after curing. The coupling efficiency is optimized by adjusting the tip position before UV curing. Because the applied glue is only a very thin layer, the coupling efficiency of the adiabatic coupler remains high (about 30% for the 1550 nm-band

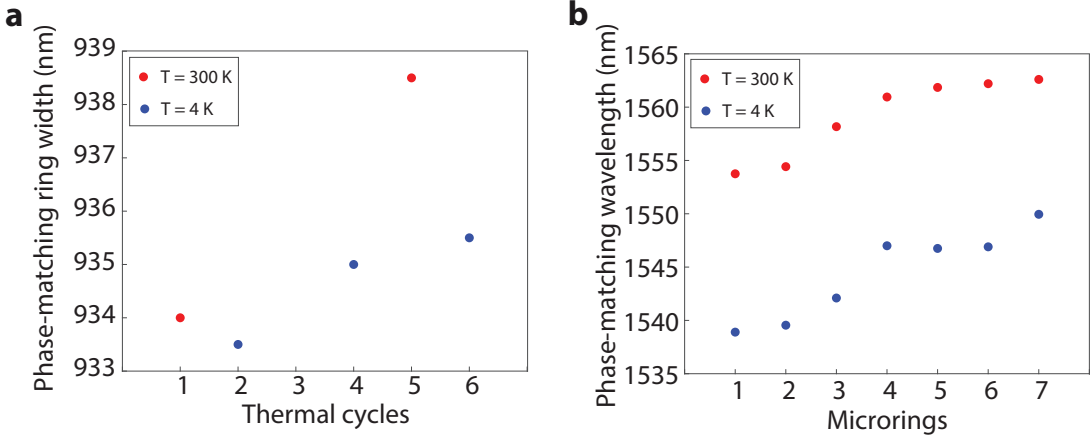


FIG. S8. **a.** The change of phase-matching ring width of one chip during multiple temperature cycles. **b.** The shift of the 1550 nm band phase-matching resonance wavelength in multiple chips from 300 K to 4 K.

light). Next we applied a large bead of glue on the edge of the chip to fix the fiber and let the glue to flow by a few mm along the fiber before UV curing. For this, we used medium viscosity, low outgassing optical adhesive (Norland NOA 88, refractive index 1.56). Finally, the chip is heated to 50 C for 12 hours for aging of the glue to achieve the optimum adhesion.

VII. DATA ANALYSIS

A. Nonlinear mode coupling

For the microring cavity that supports a pair of phase- and frequency-matched fundamental and second-harmonic resonances with frequency ω_a and ω_b , respectively, the interaction Hamiltonian between the two resonances is given by

$$\hat{H}_{\text{int}} = \hbar g(\hat{a}^{\dagger 2}\hat{b} + \hat{a}^2\hat{b}^{\dagger}). \quad (\text{S45})$$

In the pump non-depletion region, the normalized SHG efficiency, $\eta \equiv \frac{\nu_{\text{SHG}}}{\nu_{\text{in}}^2}$, where ν_{SHG} and ν_{in} are the on-chip SHG and pump power, respectively, is given by

$$\eta = g^2 \frac{\kappa_{b,e}/2}{\Delta_b^2 + (\kappa_b/2)^2} \left(\frac{\kappa_{a,e}}{\Delta_a^2 + (\kappa_a/2)^2} \right)^2 \frac{\hbar\omega_b}{(\hbar\omega_a)^2}, \quad (\text{S46})$$

where $\kappa_{a(b)} \equiv \kappa_{a(b),e} + \kappa_{a(b),i}$, $\kappa_{a(b),e}$ and $\kappa_{a(b),i}$ are the total, external and intrinsic photon (energy) loss rate of the resonances, respectively, $\Delta_a = \omega_a - \omega_p$, $\Delta_b = \omega_b - 2\omega_p$, and ω_p is the frequency of the pump. We have used the fact that the fundamental 1550 nm-band resonance is split standing-wave resonances and they couple to the even 775 nm-band resonance, regardless whether the latter is split or not. The 775 nm-band photonic crystal mirror has a weak reflection and thus only one direction of the emitted SHG light is detected. The second-harmonic cavity photon number is given by

$$\begin{aligned} \bar{n}_{c,\text{SH}} &= \frac{g^2}{\Delta_b^2 + (\kappa_b/2)^2} \left(\frac{\kappa_{a,e}/2}{\Delta_a^2 + (\kappa_a/2)^2} \right)^2 \frac{P_{\text{in}}^2}{(\hbar\omega_a)^2} \\ &= \frac{g^2 \bar{n}_c^2}{\Delta_b^2 + (\kappa_b/2)^2}, \end{aligned} \quad (\text{S47})$$

where \bar{n}_c is the cavity photon number (of the pump).

The phase-matched resonance at 1539.914 nm is tuned close to the critical-coupling condition when performing the SHG measurement. At this condition, the split between the two transmission dips is much smaller than the cavity

linewidth, and thus we used the single-resonance transmission coefficient formula $|t_\omega|^2 = \left| \frac{(\kappa_e - \kappa_i)/2 + i(\omega - \omega_0)}{(\kappa_e + \kappa_i)/2 - i(\omega - \omega_0)} \right|^2$ to fit the resonance transmission spectrum. The internal and external quality factors are extracted to be $Q_{a,i} \approx Q_{a,e} \approx 2.5 \times 10^5$. The 775-nm TM_{00} resonance is designed to be highly under-coupled, and we find $Q_{b,i} \approx 5.0 \times 10^4$ and $Q_{b,e} \approx 2.0 \times 10^6$. Based on the measured circuit efficiency (Section III) and the SHG efficiency of $105000 \pm 13360\%/\text{W}$ according to Fig. 2e, the nonlinear mode coupling rate is then found to be $g/2\pi = 6.5 \text{ MHz}$. This value is consistent with the coupling rate measured in Ref. [3], wherein the coupling rate is referred to that of the non-split resonances which differs by a factor of $\sqrt{2}$ from the split one in theory.

B. Tuning minimum transmission

The minimum transmission coefficient for waveguide phase φ has the relation $t_{\min} \propto \Delta\varphi = \varphi - \varphi_0$, where φ_0 corresponds to $t_{\min} \approx 0$. Since $\Delta\varphi \propto \Delta T \propto \Delta(V^2)$, we have $t_{\min}^2 \propto (\Delta(V^2))^2$, where ΔT is the temperature increase relative to T_0 at the phase shifter and V is the voltage applied to the phase shifter. The data in Fig. 2g is fitted using $t_{\min}^2 = \lambda(V^2 - V_0^2)^2$, where λ and V_0 are fitting parameters.

C. Second-order correlation function

Due to the presence of the residual thermomechanical noise, the output light from the device is a combination of coherent transported photons and thermomechanical noise [5], which is expressed as

$$a_{\text{out}} = t_\omega a_s + u a_m, \quad (\text{S48})$$

where a_s and a_m are the annihilation operators corresponding to the transported signal and thermomechanical noise, respectively, t_ω is the transmission coefficient, and u is the relative amplitude of the thermomechanical noise. The measured second-order correlation function of the total output state is given by

$$\begin{aligned} g^{(2)}(\tau) &= \frac{\langle a_{\text{out}}^\dagger(0) a_{\text{out}}^\dagger(\tau) a_{\text{out}}(\tau) a_{\text{out}}(0) \rangle}{\langle a_{\text{out}}^\dagger(0) a_{\text{out}}(0) \rangle^2} \\ &= \frac{|t_\omega|^4 g_s^{(2)}(\tau) + |u|^4 g_m^{(2)}(\tau) + 2|t_\omega u|^2 g_s^{(1)}(\tau) g_m^{(1)}(\tau) \cos(\omega_m \tau) + 2|t_\omega u|^2 g_s^{(1)}(0) g_m^{(1)}(0)}{(|t_\omega|^2 + |u|^2)^2} \\ &= (g_s^{(2)}(\tau) - 1) \frac{|t_\omega|^4}{(|t_\omega|^2 + |u|^2)^2} + (g_m^{(2)}(\tau) - 1) \frac{|u|^4}{(|t_\omega|^2 + |u|^2)^2} + \frac{2|t_\omega u|^2}{(|t_\omega|^2 + |u|^2)^2} g_m^{(1)}(\tau) \cos(\omega_m \tau) + 1, \end{aligned} \quad (\text{S49})$$

where $g_{s(m)}^{(1)}(\tau)$ and $g_{s(m)}^{(2)}(\tau)$ are the first-order and second-order correlation functions of the signal(thermomechanical noise), respectively, and ω_m is the frequency of the radiation-pressure-coupled mechanical mode. We have used $g_s^{(1)}(\tau) = 1$, $g_m^{(1)}(\tau) = e^{-\gamma_m \tau/2}$, and $g_m^{(2)}(\tau) = 1 + e^{-\gamma_m \tau}$, where γ_m is the dissipation rate of mechanical mode. We only keep one mechanical mode in the fitting because the dominant thermomechanical noise is originated from the ring breathing mode whose frequency is about 250 MHz according the simulation. The thermomechanical noise is universal for both phase-matched and unmatched microrings. Fig. S9 shows the measured $g^{(2)}$ for a phase-unmatched microring. The oscillation of $g^{(2)}(\tau)$ matches the frequency of the breathing mode.

Since the correlation $g_s^{(2)}(\tau)$ of the signal due to the photon-photon interaction in the $\chi^{(2)}$ cavity has a much shorter time scale ($\sim 1/\kappa_a$) compared to the period of the mechanical mode, we can use the last two terms in Eq. S49 to fit the measured $g^{(2)}(\tau)$ for $\tau \gg 1/\kappa_a$ to obtain the ratio $|u/t_\omega| \approx 0.5$. Then we use this information and the full Eq. S49 to fit the whole $g^{(2)}(\tau)$ with

$$g_s^{(2)}(\tau) = \frac{|t_\omega^2 + T(\omega, \tau)|^2}{|t_\omega^2|^2}. \quad (\text{S50})$$

Based on the theory of Section IC, we used the following phenomenological model for the phase-matched resonance in the linewidth-unresolved split situation,

$$t_\omega = r - \frac{i\kappa_{a,e}}{\omega - \omega_{\min} + i\kappa_a/2}, \quad (\text{S51})$$

$$T(\omega, \tau) = -\frac{g^2 \kappa_{a,e}^2}{(2\omega - \alpha_b)(\omega - \alpha_a)} e^{-i|\tau|(\alpha_a - \omega)}, \quad (\text{S52})$$

where ω_{\min} is the frequency corresponding to t_{\min}^2 , $\alpha_{a(b)} = \omega_{a(b)} - i\frac{\kappa_{a(b)}}{2}$, and we assumed $\omega_b = 2\omega_a$. We define minimum transmission-signal detuning $\delta \equiv \omega - \omega_{\min}$ and minimum transmission-cavity detuning $\Delta \equiv \omega_a - \omega_{\min}$. We used global fitting to fit the measured $g^{(2)}(\tau)$ at different transmission level $|t_{\omega}|^2$, by treating $\kappa_{a,i}$ as a global fitting parameter while δ , Δ , $\kappa_{a,e}$ as variable fitting parameters.

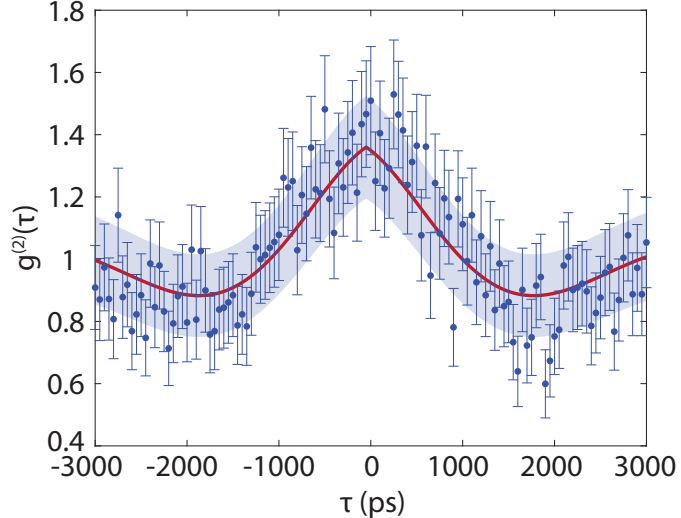


FIG. S9. Measured $g^{(2)}(\tau)$ of a phase-unmatched resonance.

[1] Shanshan Xu and Shanhui Fan, “Input-output formalism for few-photon transport: A systematic treatment beyond two photons,” *Physical Review A* **91**, 043845 (2015).

[2] Yunkai Wang and Kejie Fang, “Few-photon transport via a multimode nonlinear cavity: theory and applications,” *Physical Review A* **105**, 023713 (2022).

[3] Mengdi Zhao and Kejie Fang, “InGaP quantum nanophotonic integrated circuits with 1.5% nonlinearity-to-loss ratio,” *Optica* **9**, 258–263 (2022).

[4] J Komma, C Schwarz, G Hofmann, D Heinert, and R Nawrodt, “Thermo-optic coefficient of silicon at 1550 nm and cryogenic temperatures,” *Applied Physics Letters* **101**, 041905 (2012).

[5] Mengdi Zhao and Kejie Fang, “Observation of photon-phonon correlations via dissipative filtering,” *Physical Review Applied* **18**, 034043 (2022).

[6] Michael L Gorodetsky and Ivan S Grudinin, “Fundamental thermal fluctuations in microspheres,” *JOSA B* **21**, 697–705 (2004).